WALLFLOWER, an Arabidopsis receptor-like kinase, is polarized in root epidermal cells where it represses cell elongation impacting root waving

Patricio Pérez-Henríquez [1,2], Jessica N. Toth[1,3], Cecilia Rodriguez-Furlan[3,‡], Rachel E. De La Torre[3], and Jaimie M. Van Norman[2,3]*

[1] These authors contributed equally to this work.

[1] Department of Molecular, Cell and Developmental Biology, University of California, Los Angeles, CA, 90095, USA.
[3] Institute of Integrated Genome Biology and Department of Botany and Plant Sciences, University of California, Riverside, CA 92521, USA.
‡ Current Address: School of Biological Sciences, Washington State University, Pullman, WA 99164, USA
* Corresponding author: jaimievannorman@ulca.edu

Running title: WALLFLOWER polarity & function in cell elongation

Nutrient and water uptake relies on the ability of roots to grow through and explore the soil. When roots are grown on the surface of a substrate, growth occurs with an undulating trajectory known as root waving, which is likely due to a combination of gravity and touch responses. However, the cellular and molecular details behind root waving, remain obscure. We identified WALLFLOWER (WFL), a transmembrane receptor kinase that influences the shape of waves during root growth. WFL fused to green fluorescent protein (WFL-GFP) strongly accumulates in the root elongation zone where it is localized to the inner polar domain of epidermal cells. *wfl* mutants have longer hypocotyls and altered root waving with deeper waves. Morphometric imaging revealed that specific root epidermal cell types are longer in the mutant. Abnormal *wfl* phenotypes are rescued by WFL-GFP, but not by a truncated version of WFL missing its intracellular domains. Unexpectedly, this truncated version of WFL remains polarly localized but accumulates at the opposite (outer) polar domain. This indicates the WFL kinase domain is crucial for function and correct localization and suggests that WFL may operate locally. Altogether, we demonstrate that WFL, a polarly localized receptor-like kinase, represses cell elongation and that root waving is impacted by specific alterations in cell elongation. This study indicates that protein polarization to lateral domains in root cells is linked to precise control of longitudinal cell elongation.

INTRODUCTION

Plant development hinges on continuous organ formation and adaptive morphogenesis, producing flat leaves to capture light and directional root growth for nutrient uptake. These attributes result from refined molecular mechanisms that spatiotemporally coordinate cell division and elongation (Bouchez et al., 2024; Yi et al., 2025). These mechanisms include a complex interplay between hormone, transcriptional, and cell polarity-based signaling. Cell polarity is defined as the asymmetric distribution of any cellular component, including protein accumulation to specific intracellular or membrane regions to exert local control of biological processes (Van Norman, 2016; Ramalho et al., 2021; Jaillais et al., 2024). Polarized protein accumulation is required for many processes, including: directional transport (Janacek et al., 2024; Pérez-Henríquez et al., 2025), leaf and root patterning (Yoshida et al., 2019; Guo et al., 2021), polar cell growth (i.e. root hair formation) (Denninger et al., 2019), and tropic responses (Han et al., 2021). Proteins with polar localization may be soluble, membrane-associated, or membrane-spanning in nature. Leucine-rich repeat receptor-like kinases (LRR-RLKs) are transmembrane proteins broadly predicted to relay extracellular information into the cell to inform various developmental and immune processes (Bender and Zipfel, 2023). A small number of polarly-localized LRR-RLKs have been identified and shown to function in root cell division and specialization (Pfister et al., 2014; Alassimone et al., 2016; Campos et al., 2020; Rodriguez-Furlan et al., 2022; Goff et al., 2023; Chang et al., 2024; Rony et al., 2024).

The Arabidopsis root is an excellent system for studying cell polarity-based developmental and growth events including cell proliferation, elongation, and specialization/maturation. These processes occur in the root's longitudinal axis at defined regions: meristematic, elongation, and differentiation zones (**Figure 1A**). In the transverse axis, root cells are organized in concentric rings around the central stele and are restricted in files of cells through the longitudinal axis. This organization allows for straightforward examination of cellular phenotypes and definition of specific polarity domains within cells. In a longitudinal view of the root, cells display four broad polarity domains: shootward, rootward, inner, and outer (**Figure 1A**) (Dettmer and Friml, 2011; Van Norman, 2016; Ramalho et al., 2021; Jaillais et al., 2024). In transverse sections, the circumferential polar domain is also defined between adjacent cells in a ring (Ramalho et al., 2021). The spatial and directional information imparted by partitioned cellular components can be used by the root cells to direct cell division orientation and expansion during growth (Dong et al., 2023).

Root growth 'behaviors' are an outcome of developmental events, like cell division and elongation, being differentially modulated in response to a changing or heterogeneous soil environment (Robbins and

Dinneny, 2018; Wheeldon et al., 2022). In soil, roots often grow in a three-dimensional spiral pattern and can change growth direction or rate in response to obstacles, altered nutrient or moisture content, and/or the presence of biotic or abiotic stressors. When grown on the surface of a slightly inclined substrate, roots display sinusoidal waving, initially proposed to result from the integration of gravitropic and thigmotropic (touch) responses (Okada and Shimura, 1990; Oliva and Dunand, 2007; Sedbrook and Kaloriti, 2008). More recent theoretical frameworks suggest the importance of passive elasticity (Porat et al., 2024) and buckling of the elongation zone (Thompson and Holbrook, 2004; Zhang et al., 2022). However, the details behind sinusoidal root growth at a cellular level remain unknown.

Here, we identify an LRR-RLK that we named WALLFLOWER (WFL) due to its laterally polar accumulation in various root cell types. Specifically, WFL is polarly localized to the inner polar domain of epidermal cells in the elongation zone, where it represses non-hair cell elongation and impacts root waving. Strikingly, removing the intracellular domains of WFL results in its accumulation at the opposite (outer) polar domain. However, this truncation completely disrupts WFL function, suggesting full length WFL functions specifically where it accumulates. We contextualize these findings in the framework of cell wall asymmetries (Kelly-Bellow et al., 2023) and propose that WFL operates locally at the inner walls of epidermal cells to balance loosening of the thinner inner and thicker outer walls during elongation. Overall, our work provides evidence for the importance of lateral cell polarity-based information in modulation of longitudinal cell elongation.

RESULTS

WFL-GFP is polarly localized in root epidermal cells

WFL is closely related to other polarized LRR-RLKs, including KINASE ON THE INSIDE (KOIN, Figure **S1A**) (Rodriguez-Furlan et al., 2022). To examine WFL accumulation, we performed confocal imaging on roots expressing WFL-GFP from the endogenous *WFL* promoter (*pWFL:WFL:GFP)*, which showed WFL-GFP accumulates strongly in the root elongation zone and mildly in the meristem (**Figure 1B, left**). In the meristematic zone, WFL-GFP accumulates in epidermal hair cells and the outermost layer of the lateral root cap (LRC). In the elongation zone, WFL-GFP accumulates most strongly in the pericycle and hair and non-hair epidermal cells and is weakly detected in the cortex (**Figure 1B and Figure S1C**). The WFL-GFP accumulation pattern we observe is consistent with the transcript levels obtained from the single cell root atlas (**Figure S1B**) and aligns with our reporter for *WFL* promoter activity (*pWFL:erGFP*, **Fig S1C**).

102 In addition to accumulation in specific root developmental zones and cell types, WFL-GFP showed clear
103 polar accumulation in outer cell types. In the lateral root cap, WFL-GFP accumulates to the inner polar
104 domain of the plasma membrane (PM) (**Figure S1C**). In epidermal hair cells of the late (shootward)
105 meristem, WFL-GFP preferentially accumulates at the circumferential polar domain (**Figure 1B**), while in
106 the elongation zone, WFL-GFP accumulates at the circumferential and inner polar domains of all
107 epidermal cell types (**Figure 1B**). Importantly, polar accumulation of WFL-GFP is also observed upon
108 misexpression with cell layer-specific promoters. For instance, WFL-GFP accumulates at the
109 circumferential polar domains in epidermal cells in the shootward (late) meristem when expressed under
110 the *WEREWOLF* promoter (*pWER)*, whereas it accumulates at the circumferential and inner polar
111 domain when specifically expressed in the endodermis *(pSCARECROW, pSCR)* and maturing cortex
112 (*pCORTEX1, pC1*) (**Figure 1C**). This suggests that WFL polar accumulation doesn't depend on cell
113 identity and is informed, in part, by cell developmental stage. Altogether, the spatiotemporal-specific
114 accumulation of WFL suggests a link between its polar localization and WFL function at different root
115 developmental stages.
116
117 **WFL function impacts root waving**
118 To determine the function of WFL, we targeted *WFL* (At5g24100) for mutagenesis via CRISPR-Cas9
119 (Fauser et al., 2014). The *wfl-1* allele shows reduced *WFL* expression (**Figure S1D**) and is likely a null
120 allele due to a premature stop codon early in the coding sequence (see methods section for details). We
121 used WFL accumulation to guide our phenotypic analysis with WFL-GFP in the pericycle prompting us to
122 examine lateral root production in *wfl*, however, no change in lateral root density was observed (**Figure**
123 **S1E**). Accumulation of WFL-GFP at the transition between meristem and elongation zones, and the shift
124 in its polar localization, suggested WFL might function at this transition. We were unable to detect a
125 difference in total root length between Columbia-0 (Col-0) and *wfl* single mutant, or any additive root
126 length phenotype in the double mutant between *wfl* and a mutant allele of *WALLFLOWER RELATED 1*
127 (*WFLR1*, At5g53320, Salk_128780) (**Figure 1E and Figure S1E-G**) indicating these closely related
128 receptors are not functionally redundant for overall root length. After further examination of *wfl* root
129 growth, we noticed altered root waving compared to wild type (Col-0). This difference was exacerbated
130 by growing seedlings on plates inclined 20˚. To further characterize this, we quantified the most
131 descriptive root wave features (Oliva and Dunand, 2007), the wave amplitude and wavelength (**Figure**
132 **1D-E**). This showed that *wfl* root waves have a higher amplitude but similar wavelength, meaning that
133 root waves are generated at the same frequency in *wfl* but grow deeper, suggesting a difference in cell
134 elongation during growth. This abnormal waving phenotype is rescued by endogenous expression of
135 WFL-GFP (**Figure 1D-E**) demonstrating that WFL functions to modulate root waving. Normal root length
136 but deeper root waves in *wfl* implies a transient or very local function for WFL in the root.

137

138 **WFL functions to repress cell elongation**

139 Root waves result from the modulation of elongation dynamics and perhaps the buckling of the
140 elongation zone because it is more elastic and not anchored to the substrate (Thompson and Holbrook,
141 2004; Zhang et al., 2022). Epidermal growth control theory states that peripheral cell layers determine
142 the elongation rate of an organ (Kutschera and Niklas, 2007). Given that WFL-GFP strongly accumulates
143 in the elongation zone and not mature regions of the root (**Figure S2A**), we hypothesized that loss of
144 WFL impacts root waving due to abnormalities in epidermal cell elongation. To test this, we performed *in*
145 *situ* imaging to measure epidermal cell length while preserving positional information within root waves.
146 After staining with propidium iodide (PI), multiple high magnification z-stack images were acquired,
147 stitched together, and processed with MorphoGraph X (MGX) to project the surface signal into a 2D
148 image (**Figure 2A**). This approach allowed us to distinguish curved peak regions from straight interwave
149 regions and hair from non-hair cells in Col-0, *wfl*, and *wfl pWFL:WFL:GFP* roots (**Figure 2B**). With these
150 projections, we measured individual epidermal cell lengths in the longitudinal axis. Consistent with
151 previous reports, we found hair cells were slightly shorter and more variable in length than non-hair cells
152 (Grierson et al., 2014). More importantly, hair cell length in *wfl* and wild type were similar in peak and
153 interwave regions (**Figure 2C**), while non-hair cells were consistently longer in *wfl*. This longer non-hair
154 cell phenotype was rescued by the endogenous expression of WFL-GFP (*wfl, pWFL:WFL:GFP*),
155 suggesting WFL represses non-hair cell elongation.

156

157 To examine WFL's role in cell elongation more generally, we measured hypocotyl length. Seedlings were
158 grown on media without sucrose in dim light conditions, to induce hypocotyl growth based solely on cell
159 elongation. In these conditions, *wfl* seedlings had longer hypocotyls than wild type (Col-0) and
160 expression of WFL-GFP rescued this hypocotyl phenotype (**Figure 2D**). Additionally, seedlings
161 overexpressing WFL (Col-0, *pWFL:WFL:GFP*, Figure **S2B**), had shorter hypocotyls than wild type after
162 exposure to dim light (**Figure 2D**). This suggests WFL activity in repression of cell elongation is dose
163 dependent. We detected WFL-GFP only at the rootward end of hypocotyls when expressed in *wfl* or in
164 Col-0 (**S3A-B**). Additionally, we found no difference in hypocotyl cell length, root length, or root growth
165 rate in *wfl* compared to Col-0 on sucrose-free media under standard light conditions (**Figure S3C-E**).
166 This indicates there is no difference in hypocotyl cell number or length due to changes in embryonic
167 development, but instead that hypocotyl length differences arise during dim light-induced cell elongation.
168 The hypocotyl phenotypes when WFL is absent or abundant are consistent with its role in repressing cell
169 elongation, particularly in conditions that induce more dramatic elongation.

170

171 Prompted by the hypocotyl phenotype in Col-0 seedlings expressing WFL-GFP, we closely examined the
172 roots of these seedlings and found a slight root hair positioning defect. Root hairs typically initiate and
173 grow out at a very defined distance above an epidermal cell's rootward end (Denninger et al., 2019).
174 However, upon *WFL-GFP* overexpression, a higher frequency of root hairs initiate and grow out in
175 parallel with the cell's rootward end (**Figure S2C-D**) with no other root hair defects observed. We could
176 not detect any root hair positioning defect in *wfl* mutants. To rule out the possibility that the downward
177 shift in root hair position was due to some interference of GFP fused to WFL, we expressed WFL in Col-0
178 without a GFP tag and found the same shift in root hair position (**Figure S2E**). Root hair initiation
179 requires substantial cell wall loosening at a particularly specific position. These results suggest excess
180 WFL interferes with normal positioning of root hair formation, perhaps by disrupting the specific position
181 of cell wall loosening. Altogether, our findings on root epidermal cell length, hypocotyl length, and root
182 hair positioning are consistent with a context-specific role for WFL in modulating cell elongation.
183

184 **WFL represses longitudinal anticlinal divisions of hair cells in the root meristem**

185 Cells in the root meristem primarily undergo proliferative cell divisions and WFL localizes to the
186 circumferential polar domain of epidermal hair cells in the root meristem. Our previous work showed that
187 other LRR-RLKs in this subfamily, namely IRK and KOIN, function to repress cell division frequency
188 and/or orientation in the root meristem (Campos et al., 2020; Rodriguez-Furlan et al., 2022; Rony et al.,
189 2024), leading to the hypothesis that WFL may also have a role in cell division. To determine differences
190 in epidermal cell division in *wfl*, we performed 3D confocal imaging of root meristems (Campos and
191 Van Norman, 2021), which allowed us to examine cell division orientation and frequency throughout the
192 meristem (**Figure 3A**). After careful examination, we detected more frequent longitudinal anticlinal
193 divisions (LAD) in the *wfl* epidermis, which result in bifurcation of one cell file into two. By examining
194 intersecting *xy* and *xz* planes, we found that epidermal hair cells divide to produce additional non-hair
195 cells, as the new cells contact just one underlying cortex cell. The frequency of bifurcated cell files is
196 restored to wild-type levels by expression of *pWFL:WFL:GFP* in *wfl* (**Figure 3B-D**). The increase in the
197 number of non-hair cell files through hair cell division is a typical patterning strategy in Arabidopsis roots
198 after germination (Berger et al., 1998). Consistently, 50% of wild type (Col-0) roots at 3 dps (days post
199 stratification) display these epidermal LADs but we observe them in 100% of *wfl* roots. Interestingly, a
200 similar bifurcation of epidermal cell files was also observed in *wfl* hypocotyls at 3 dps, again at a higher
201 frequency than observed in wild type (**Figure 3E-F**). This increase in epidermal cell number in the radial
202 axis had no impact on hypocotyl width (**Figure S3F**). These data suggest that in the absence of WFL,
203 epidermal cells in the root and hypocotyl execute longitudinal anticlinal divisions more frequently than
204 normal.
205

206 **WFL-GFP is trafficked to plasma membrane by targeted exocytosis**

207 Proteins with polar localization can be directed to the PM by targeted exocytosis and/or maintained at the
208 PM by endocytosis and recycling (Rodriguez-Furlan et al., 2019; Raggi et al., 2020). To investigate how
209 endomembrane trafficking contributes to WFL-GFP polar distribution, we examined its accumulation in
210 roots following a series of chemical treatments. Brief treatment with Brefeldin A (BFA), an inhibitor of
211 Golgi trafficking that affects exocytosis to the PM, generated intracellular agglomerations consistent with
212 BFA bodies (**Figure S4A, left**). These could correspond to endocytosed WFL arriving at the trans-Golgi
213 network to be recycled or exocytosis of newly synthesized protein. To distinguish between these options,
214 roots were treated with cycloheximide (CHX), a protein synthesis inhibitor and, after just 2 hours,
215 WFL-GFP signal at the PM was considerably reduced. Thus, the majority of WFL-GFP in BFA bodies
216 can be attributed to trafficking of newly synthesized protein. We also found that pretreatment with CHX
217 dramatically reduced BFA-agglomerations and BFA wash out in the presence of CHX showed recovery
218 of WFL-GFP signal at the PM suggesting a proportion of WFL, however small, is constantly recycling
219 (**Figure S4A, right**). Because darkness induces internalization and trafficking of PM proteins to the
220 vacuole and delays their luminal degradation allowing GFP detection at the vacuole lumen (Kleine-Vehn
221 et al., 2008), we used a 3-hour dark treatment and detected increased WFL-GFP at the lumen in
222 epidermal cells (**Figure S4B**). We next explored how WFL-GFP accumulation in darkness is impacted by
223 Wortmannin (Wm), an inhibitor of phosphoinositide synthesis widely used to inhibit the endocytic
224 trafficking of receptors from the PM towards the vacuole for degradation. The 2-hour Wm-treatment in
225 darkness, revealed WFL-GFP in characteristic doughnut-shaped intracellular accumulations and
226 considerable decrease in fluorescent signal at the vacuole lumen. Together, these results suggest WFL
227 has a high turnover rate, being synthesized and degraded in a short time.

228

229 **WFL requires its kinase domain for its normal polarity and function**

230 Like other LRR-RLKs with polar accumulation that we have identified, WFL is classified as an atypical
231 kinase (Castells and Casacuberta, 2007). Nonetheless, the kinase domain of KOIN is required for its
232 function and polar accumulation at the PM, whereas the IRK kinase domain is largely dispensable for its
233 polar accumulation and function (Campos et al., 2020; Rodriguez-Furlan et al., 2022). Therefore, we
234 asked if WFL's localization and/or function is affected by removal of its juxtamembrane (Jx) and kinase
235 (K) domains (**Figure 4A**). We observed that roots expressing *pWFL:WFLΔJxK:GFP* showed strong
236 accumulation of WFLΔJxK:GFP in the elongation zone similar to full length WFL-GFP (**Figure 4B**).
237 Strikingly, transverse optical sections revealed that WFLΔJxK-GFP accumulates at the opposite side of
238 epidermal cells - residing at the outer polar domain and the circumferential polar domain (**Figure 4C**). In
239 the root tip, WFLΔJxK-GFP also accumulates at the outer polar domain of meristematic epidermal cells
240 and cells of the LRC (**Figure S5A**). Furthermore, misexpression with cell layer-specific promoters

241 showed that truncated WFL predominantly localizes to the circumferential and outer polar domain of
242 many root cell types, except the endodermis, where it has nonpolar accumulation (**Figure S5B-C**). This
243 is consistent with WFL polarization at the plasma membrane being informed by an organ-level cue
244 generally orienting WFL towards or away from the stele.
245
246 While closely examining WFL∆JxK-GFP accumulation at the outer polar domain of epidermal cells, we
247 noticed that it was conspicuously absent from sites of root hair formation. Given this and the downward
248 shift in root hair positioning upon WFL overexpression, we compared the accumulation of WFL- and
249 WFL∆JxK-GFP during root hair formation. We found WFL-GFP accumulates specifically at the center of
250 root hair initiation sites and bulges, but not on the rootward or shootward sides of a root hair (**Figure**
251 **4D-E).** In contrast**,** WFL∆JxK-GFP is specifically diminished at the center of root hair initiation sites and
252 bulges. This mirrored polarized accumulation in root hairs matches our observations of how these
253 proteins accumulate at opposing polar domains of cells in the elongation zone and is an unexpected
254 consequence of WFL kinase domain deletion (**Figure 4F)**. Finally, we assayed hypocotyl elongation to
255 determine whether WFL∆JxK-GFP was functional and found that, unlike full length WFL-GFP, it was
256 unable to rescue *wfl* (**Figure 4G)**. These results indicate that the WFL kinase domain is not required for
257 polarized accumulation in general, but that this domain plays a crucial role in WFL localization to the
258 inner polar domain of root cells and is essential for WFL-driven repression of cell elongation.
259
260 **DISCUSSION**
261 This work finds that WFL, a transmembrane receptor kinase, is polarly localized to the inner side of
262 elongating epidermal cells and functions to repress cell elongation, leading to altered root waving. We
263 propose that during elongation, WFL acts to balance the intrinsically different properties of the inner
264 and outer walls of epidermal cells, acting locally at the inner side.
265
266 **Mechanisms for WFL polar accumulation**
267 The mechanisms underlying WFL polarization are intriguing. WFL localization shows a dual polarity
268 being present at the inner side of epidermal cells and at specific places on the outer side during root
269 hair formation. This could be achieved through nonpolar trafficking of WFL to the entire PM and then
270 selective removal. However, non-polar localization of WFL was not detected. We consistently detected
271 polarly localized WFL in every developmental stage and upon treatment with BFA or Wortmannin. This
272 suggests that polar localization of WFL is achieved by targeted exocytosis. Indeed, other LRR-RLKs
273 that we have previously characterized, namely IRK and KOIN, are also polarly localized by targeted
274 exocytosis. However, IRK and KOIN polar localization is achieved through distinctive pathways *i.e.*
275 sensitive and insensitive to the golgi trafficking inhibitor BFA, respectively (Rodriguez-Furlan et al.,

2022). Like IRK, WFL trafficking is also BFA-sensitive; therefore, we presume they share commonalities in their polar accumulation mechanisms.

Another layer of complexity arises when examining the accumulation of WFL∆JxK, which shows a remarkable 'mirror image' of the polarity of full length WFL-GFP. This observation differs from similarly truncated KOIN and IRK, where KOIN∆JxK shows non-polar accumulation and IRK∆JxK displays correct polar accumulation (Rodriguez-Furlan et al., 2022). We interpret this to mean that a protein-intrinsic cue for polar accumulation is present in the KOIN intracellular domain and absent from the IRK intracellular domain. However, WFL∆JxK presents an additional scenario, suggesting that information for WFL polar accumulation resides in its extracellular and intracellular protein domains. This suggests that an expansion of the factors involved in WFL polarization is needed. For instance, WFL localization may require interaction with specific PM environments through the transmembrane and kinase domains (Pan et al., 2023). Alternatively, the WFL extracellular domains may also participate in polarization, via binding to specific extracellular or cell wall components, as proposed for other LRR-RLKs (Hématy et al., 2007; Feng et al., 2018). The mirrored polar accumulation of WFL and WFL∆JxK indicates the precise workings of protein polarization mechanisms in plants remain elusive.

Is WFL function determined by localization or intracellular domains?

In addition to WFL∆JxK polarly localizing to the opposite side of root cell types, this truncation fails to rescue *wfl* cell elongation phenotypes. This immediately suggests that the WFL intracellular domains are essential for its function, perhaps for downstream signaling. Alternatively, WFL localization may be essential for its function, for instance, because WFL∆JxK is in the wrong place - it cannot function, perhaps due to a missing interaction partner or other functional constituent. These options are not mutually exclusive and determining the functional contribution(s) of protein localization itself and/or individual domains requires a deeper understanding of WFL's polarization mechanisms, its interaction partners, and downstream targets. Dissecting these possibilities is expected to bring interesting insights to the ongoing discussion about polarization-dependent protein function (Nakamura and Grebe, 2018; Muroyama and Bergmann, 2019) in many aspects of plant growth and development.

Does WFL repress cell elongation by balancing cell wall properties?

Given the strong accumulation of WFL at the inner polar domain of elongating epidermal cells and its function to specifically repress non-hair cell elongation, it is tempting to propose that WFL represses cell elongation by inhibiting cell wall loosening. However, this hypothesis doesn't align well with WFL localization to root hair initiation sites or bulges where the cell wall is undergoing local, dramatic loosening to allow for tip growth (Vissenberg et al., 2001). Perhaps WFL represses cell elongation by

locally *promoting cell wall stiffness*, ultimately, acting to maintain cell wall integrity in the face of dramatic changes?

Epidermal cells carry striking asymmetries in the material properties of their lateral cell walls. The outer cell wall is thicker and harder, whereas the inner wall is thinner and softer. A thicker outer wall supports direct contact with the environment, with the exterior epidermal cell wall being up to 10 times thicker (Kutschera and Niklas, 2007; Dyson et al., 2014; Kelly-Bellow et al., 2023). This physical asymmetry in the wall necessitates that, during elongation, cells must balance how loose or stiff each lateral wall is such that growth can occur uniformly in the long axis. If this balance is not maintained, a cell could lose integrity or shape due to asymmetric elongation at the lateral sides. We consider that the simplest strategy for this balancing act is local and selective modification (loosening or stiffening) of the cell wall. Given that WFL natively accumulates on the softer, thinner side of epidermis during cell elongation, we propose WFL functions to repress cell elongation through local alteration of inner cell wall properties (**Figure 5**). For instance, as the entire cell wall loosens for elongation, WFL may act locally at the inner polar domain shifting that cell wall towards stiffness. Locally stiffer cell walls could also explain the higher frequency of longitudinal anticlinal divisions (LADs) in *wfl* hair cells in the late meristematic zone. Without WFL at the circumferential polar domain, the hair cells could be more susceptible to the activation of cell division by mechanical stress patterns (Hoermayer et al., 2024; Höfler et al., 2024). This could similarly apply to the cell division events we observe in the hypocotyl. We note that longitudinal anticlinal hair cell division in *wfl* generates additional non-hair cells, which would increase the number of cells that would experience increased elongation, further contributing to the deeper root wave phenotype in *wfl*.

Finally, WFL function to push the cell wall towards stiffness could also explain the more rootward position of root hairs observed upon WFL overexpression. Root hairs normally grow out from a specific area in the outer cell wall that must soften and thin (Vissenberg et al., 2001), a position where WFL accumulates. WFL at this position could help prevent excessive wall loosening, which would result in misshapen or ruptured root hairs. However, upon overexpression, excess WFL at these sites may lead to a greater stiffness in the wall; consequently, leading to displacement of some root hair bulges as the cell manages conflicting cues to loosen and stiffen the wall at this location.

In summary, our work reveals a polarly-localized receptor kinase that represses epidermal cell elongation and impacts root waving. The proposed function for WFL in altering local cell wall properties links fundamental cellular attributes (polarity and directional expansion) with organ-level growth

345 'behaviors'. Understanding how fundamental aspects of cell biology impinge on organ growth is
346 essential to improving plant productivity in agricultural settings.
347

348 **MATERIALS & METHODS**

349 **Plant materials and growth conditions**

350 The *Arabidopsis thaliana* Columbia-0 (Col-0) ecotype was used as the wild type. All seedlings were
351 grown on plates in a Percival growth chamber at 22°C under a 16 h light/ 8 h dark photoperiod with
352 60-110 µmol/m^{-2}s^{-1} of light intensity with details indicated for specific experiments. In vitro growth was
353 carried out in 1X Murashige and Skoog (MS) basal salts (Caisson Lab®, Cat. Num. MSP01), 0.05%
354 MES, 1% sucrose, pH 5.7 and 1% Agar (Difco Agar, BD®, Cat. Num. 214530), unless otherwise noted.
355 Seeds were surface sterilized with chlorine gas and stratified on plates at 4°C for 2-3 overnights and
356 then put into the growth chamber. Plants were propagated in a growth room either with 24 h light or 16
357 h light/ 8 h dark photoperiod at 20-24˚C.
358

359 **Vector Construction and Plant Transformation**

360 Transcriptional (promoter activity) and translational reporters were constructed by standard molecular
361 biology methods and utilizing Invitrogen Multisite Gateway® technology (Carlsbad, USA). A region 4.1
362 kb upstream of the *WFL* (At5g24100) start codon was amplified from Col-0 genomic DNA and
363 recombined into the Invitrogen pENTR™ 5'-TOPO(® TA vector. For *WFL* promoter activity, the
364 promoter drove endoplasmic reticulum-localized green fluorescent protein (erGFP) as previously
365 described (Van Norman et al., 2014). For translational fusions, the genomic fragment encoding *WFL*
366 from the ATG up to, but excluding the stop codon (including introns, 2.0 kb), was amplified from Col-0
367 genomic DNA and recombined into the Invitrogen pENTR™ DIRECTIONAL TOPO®
368 (pENTR-D-TOPO) vector and fused to a C-terminal GFP tag (unless otherwise noted) as previously
369 described (Van Norman et al., 2014). Specific primers for *WFL* cloning are listed in Table S1. WFL-GFP
370 and WFL∆JxK-GFP were driven by cell type-specific promoters (*pSCR$_{2.0}$, pCO$_2$, pC1, pUBQ10,* and
371 *pWER)* as previously described (Lee et al., 2006; Campos et al., 2020). Due to the relatively low
372 fluorescent signal of *pWFL:WFL∆JxK-GFP,* misexpression reporters for these truncations were
373 reconstructed with 3xYFP. *pC1* was received in (Gateway Compatible) pENTR™ P4P1R TA vector from
374 the lab of Philip Benfey, Duke University (Durham, NC, USA). The epidermal misexpressed fusion
375 protein, *pWER:WFL-eYFP:WER3',* was generated as previously described (Campos et al., 2020).
376

377 The various Gateway compatible fragments were recombined together with the dpGreen-BarT or
378 dpGreen-NorfT (Norflurazon (Norf) resistance) destination vector (Lee et al., 2006). The

379 dpGreen-NorfT vector was generated by combining the backbone of dpGreen-BarT with the
380 p35S::tpCRT1 and terminator insert from pGII0125. Within the target region of the dpGreen-BarT, one
381 AclI site was mutated with the QuickChangeXL kit (Stratagene). Plasmids were amplified in
382 ccdB-resistant *E. coli* and plasmids prepped with a Bio Basic Plasmid DNA Miniprep kit. 34 uL of the
383 modified dpGreenBarT and unmodified pGII0125 were digested with 1 µL each FspI and AclI in
384 CutSmart buffer (NEB) for 1hr at 37˚C. Digests were subjected to gel electrophoresis on a 1% agarose
385 gel. The 5866 bp fragment from the dpGreenBarT and 2592 bp fragment from the pGIIII0125 were
386 extracted with a Qiagen MinElute Gel Extraction kit. The fragments were then ligated at 1:1 volumetric
387 ratio (20ng vector; 8.8ng insert) using T4 DNA ligase incubated at 16˚C overnight before
388 transformation into ccdB-resistant *E. coli*. Expression constructs were then transformed into Col-0
389 plants by the floral dip method (Clough and Bent, 1998) using Agrobacterium strain GV3101 (Koncz et
390 al., 1992) and transformants were identified using standard methods.
391
392 For each transgenic reporter line, up to 15 independent T1s were isolated and propagated. T2 lines
393 with a 3:1 ratio of resistant:sensitive seedlings, indicating the transgene is inherited as a single locus,
394 were allowed to self (3-5 lines minimum) and among the subsequent T3 progeny, those with 100%
395 resistant seedlings, indicating that the transgene was homozygous, were used in further analyses. For
396 each reporter, at least three independent lines with the same relative expression levels and localization
397 pattern were selected for imaging by confocal microscopy.
398
399 **CRISPR-induced mutagenesis**
400 A candidate T-DNA insertional allele of *WFL* was obtained from the ABRC (Arabidopsis Resource
401 Center), SAIL_1170_A12, but was discarded as no heterozygous or homozygous mutant individuals
402 could be identified in multiple batches of seeds. An allele (*wfl-1*) was generated using CRISPR-Cas9
403 technology and used for all phenotypic analyses. CRISPR-induced mutagenesis was performed as
404 described in (Fauser et al., 2014), a single guide RNA (5'-TTTAACGGTAGTATTCCCGCGGG) was
405 selected in exon 2 of *WFL.* Single locus heritability was tested with 3:1 ratio of resistant:sensitive
406 seedlings segregation in the T2 population. These plants were subsequently examined for lesions in
407 *WFL* in proximity to the guideRNA binding site. In two individual transgenic lines, single point mutations
408 were obtained at the same position. A single T (*wfl-1)* or a single A (*wfl-2*) was inserted 486 nucleotides
409 after the start codon, which results in 4 novel amino acids and a premature stop codon. Because these
410 alleles have the same consequences on the protein coding region, generating a stop codon prior to an
411 intron and the coding region for the transmembrane domain, it is unlikely that any partially functional
412 protein could be produced; thus, we focused our analyses on *wfl-1*.
413

414 **Confocal microscopy**

415 All images were acquired with laser scanning confocal microscopes using either a Leica SP8 (housed
416 in the Van Norman lab at University of California, Riverside, UCR) or a Zeiss 980 (housed in the Van
417 Norman lab at UC, Los Angeles, UCLA) with water immersion, 40X objective, NA = 1.2. Fluorescent
418 signals were captured using the following settings: propidium iodide (PI; excitation 543/561 nm,
419 emission 580-660 nm), GFP (excitation 488 nm, emission 492-530 nm), and YFP (excitation 514 nm,
420 emission 515-550).

421

422 **2D Image processing**

423 Post-acquisition image processing was performed with proprietary software Zeiss ZEN® 3.7 software,
424 Leica Application Suite® X (LASX) software, or with the open source Fiji (Fiji is Just ImageJ) v1.54.
425 Final multi-panel figures were assembled using Adobe® Illustrator and Adobe® Photoshop. Plasma
426 membrane fluorescence intensity in chemical treatments were processed using ImageJ. The intensity
427 was corrected by background readings using the formula: Integrated Density - (Area of selected cell x
428 mean values of background readings). Plasma membrane fluorescence intensity in root hairs was
429 obtained using LASX. Position 1, 2, 3 corresponds to the area above, center or below the root hair
430 initiation domain or bulge. Measurements were performed in 2-3 cells per root in a total of 15-20 roots
431 per replicate.

432

433 **2.5 and 3D Imaging and image processing**

434 All tiled images were acquired with confocal microscope Zeiss 980 (UCLA) and processed at a
435 high-performance PC running Windows 10 Enterprise equipped with a CPU AMD Ryzen Pro 3955WX
436 with 16-cores 3.9GHz and GPU Nvidia RT A5000. Tiled images were stitched together before further
437 processing with the Zen desk v3.8 software using the processing function 'Stitching' and following
438 parameters. FUSE TILES: Yes, DIMENSION REFERENCES: All by reference (pick a z-position with
439 clear signal), EDGE DETECTOR: Yes, MINIMAL OVERLAP: 5%, MAXIMAL SHIFT: 5%, COMPARER:
440 Best, GLOBAL OPTIMIZER: Best.

441

442 Stitched images were then processed for single-channel 2.5D projections (surface projections) or
443 dual-channel 3D projections. <u>2.5D projections or surface projections</u> were calculated with
444 MorphoGraphX v2.0. For this, 16-bit images were acquired with a stepsize of 1 µm. Lower step size
445 dramatically increased the file size without improving the epidermal signal projected to the surface. The
446 analysis assisted by MGX was the following: First, images were converted from CZI to TIFF using Fiji.
447 Then, a Gaussian blur filter was used [XYZ sigma = 0.3-1.2 µm]. Voxels were edited to erase the
448 blurry noise around the image. Edge detection was run with THRESHOLD=default (10000). Then,

449 Mesh was created with the marching cubes surface process using CUBE SIZE = 5. Mesh was
450 manually trimmed eliminating mesh built at the base of the z-stack to avoid unnecessary processing in
451 the next steps. Importantly, mesh processing was two rounds of subdividing and smoothing the mesh.
452 Finally, signal was projected onto the surface with MIN DIS = 3 µm and MAX DIST = 8 µm. *3D*
453 *projections* were performed with the Arivis Vision4D v 4.1.1 software using 8-bit images acquired with a
454 step size of 0.3 µm. GFP and PI channels were visualized with Rainbow and red LUT. Images were
455 processed in Arivis with the following workflow: 3D RENDERING: Transparency, 4D OPACITY
456 SETTINGS: Opacity curves = Transparency. COLOR SETTINGS: Gamma = 1, and 4D CLIPPING:
457 plane *xz* = Invisible or Textured/Opaque.
458

459 **Scanning electron microscopy**

460 Hypocotyls from seedlings at 3 days post-stratification (dps), grown in normal light conditions, were
461 imaged using the Hitachi TM4000 Plus II with an electron gun voltage of 15 kV (at UCR). Whole
462 seedlings were displayed directly on the mounting platform on top of double-sided tape. The sample
463 was flattened down by carefully tapping down the root and the cotyledons. Images were obtained at
464 100X magnification in mixed detection mode BSE/SE which combines backscattered electron imaging
465 (BSE) and secondary electron (SE) detection. Default vacuum conditions were used as they are
466 specially designed for hydrated samples.
467

468 **Root phenotypic analyses**

469 Seedlings are grown for 5 dps at 20° inclination to enhance root waving as indicated by (Tan et al.,
470 2015). Root wave features, as described by (Oliva and Dunand, 2007), were measured in Fiji from
471 images captured on a flatbed scanner. Plates were positioned at 20˚C inclination at day 0 in the growth
472 chamber for seedling germination and growth. Root length was obtained by tracing the root with the
473 segmented line tool in ImageJ from images of the plates. Lateral root density was obtained from
474 seedlings grown vertically through the agar in plates and was calculated as the number of emerged
475 lateral roots divided by primary root length. Root hair bulge position measurements were performed on
476 seeds at 4 dps grown on 0.5 X MS media following published protocols (Masucci and Schiefelbein,
477 1994). Root hair bulges were binned into 2 categories with the following parameters: “normal” if there
478 was a measurable distance from the emerging root hair to the rootward edge of the harboring
479 epidermal cell and “rootward shifted” if there was no measurable distance.
480

481 **Hypocotyl phenotypic analyses**

482 Hypocotyl length assays were performed on seedlings growth on media without sucrose. Sucrose is
483 omitted to avoid interference with growth rates and de-etiolation response. For dim light response

484 assays, seeds were first germinated in light at 60 μmol/m^{-2}s^{-1} for 2 days, then exposed to dim light (5
485 μmol m^{-2} s^{-1}) for 4 days. Plates were positioned horizontally throughout the experiment. After dim light
486 treatment, hypocotyls are transferred to and aligned on a humid transparent plastic sheet to obtain
487 images (acquired on a flatbed scanner). Light intensity was measured with a LI-250 light meter
488 (LI-COR ®) equipped with a quantum sensor. A dim light environment was created with a plastic box
489 homogeneously wrapped in white paper.
490
491 Hypocotyl width and epidermal cell length was obtained from hypocotyl SEM images (see above) from
492 3 dps seedlings grown in normal light conditions. SEM images allowed the hypocotyl files of large
493 non-dividing cells to be distinguished from files of small cells. In Arabidopsis hypocotyls, the large
494 non-dividing cells are positioned outside of a single cortical cell file, and are characterized by the
495 expression of *GL2*, the marker for root non-hair cells (Daher et al., 2018; Gao et al., 2022). Hypocotyl
496 width measurements were made at the rootward, center, and shootward regions of the hypocotyl and
497 then values were aggregated for the quantification shown.
498
499 **Chemical Treatments**
500 Treatments with small molecules were performed using *pWFL:WFL-GFP* in the Col-0 background
501 seedlings grown on 0.5x MS plates grown for 5 dps. Seedlings were then incubated in liquid 0.5x MS
502 containing one or a combination of the following chemicals: Brefeldin A (BFA, Sigma-Aldrich) was
503 dissolved in dimethyl sulfoxide (DMSO, Calbiochem, Cat #317275) in 50 mM stocks and added to the
504 media at a final concentration of 50 μM for 1 hour or other indicated times. Cycloheximide (CHX,
505 Sigma-Aldrich, Cat #C7698) was dissolved in DMSO and added from a 50 mM aqueous stock to a final
506 concentration of 50 μM for 2 hours or other indicated time. Wortmannin (Wm, Sigma-Aldrich) was
507 dissolved in DMSO and used at 33 μM for 2 hours. In control (mock) experiments, seedlings were
508 incubated in the same media containing an equal amount (0.05% to 0.1%) of the solvent. Washout was
509 performed by transferring seedlings to new 0.5x MS media containing one or more of the treatments as
510 described in the results section.
511
512 **qRT-PCR Analysis**
513 RNA was isolated with Qiagen's RNeasy Plant Mini Kit from whole seedlings at 7 dps from three
514 independent biological replicates. First-strand cDNA was synthesized from 1 μg total RNA with
515 RevertAid First Strand cDNA Synthesis and the oligo(dT)$_{18}$ primer (Thermo Scientific). qRT-PCR
516 reactions were set up in technical replicates using IQ SYBR Green Supermix (BioRad). Cycling
517 conditions: 95°C for 3 min followed by 40 cycles of 95°C for 10s and 57°C for 20 s. Standard curves
518 were performed at least in duplicate. Primer efficiencies were measured as 90-110% for all primers.

See Table S1 for primer sequences. Transcript levels were calculated using the software CFX Manager (Bio-Rad), normalizing to *PP2A*/AT1G13320 (Czechowski et al., 2005).

Statistical analysis

All pairwise comparisons were performed with GraphPad Prism 10 (www.graphpad.com) or ggplot2 (https://ggplot2.tidyverse.org) package in RStudio, for parametric (*t*-test) and non-parametric analysis (Wilcoxon). Multiple comparison one-way ANOVA with Dunn's multiple comparisons post-test was used in GraphPad Prism 10 (www.graphpad.com).

DATA AVAILABILITY

The WALLFLOWER (WFL) accession number is At5g24100 and the WALLFLOWER-RELATED 1 (WFLR1) accession number is At5g53320. The data and plant and molecular materials underlying this article will be shared on reasonable request to the corresponding author.

FUNDING

The initial stages of this work was supported by Initial Complement (IC) funds from the University of California, Riverside, USDA-NIFA-CA-R 587 BPS-5156-H, NSF CAREER award #1751385 to J.M.V.N., and NSF-GRFP award #DGE 588 1326120 to J.N.T. Support for the phenotypic analyses and 3D imaging came from Initial Complement (IC) funds from the University of California, Los Angeles.

AUTHOR CONTRIBUTIONS

Initial stages of the work at UC Riverside: Conceptualization: J.M.V.N.; Methodology and Investigation: J.M.V.N., J.N.T., and C.R-F.; Resources: J.M.V.N. and J.N.T.; Writing - first manuscript (posted in BioRxiv): J.N.T., C.R-F., and J.M.V.N.; Visualization: J.N.T. and C.R-F.; Supervision: J.M.V.N.; Funding Acquisition: J.M.V.N. and J.N.T.

Later stages of work at UC Riverside and UC Los Angeles: Conceptualization: P.P-H. and J.M.V.N.; 3D imaging: P.P-H.; *wfl* phenotypic analysis: P.P-H, R.E.D.; Double mutant analysis *wfl* and related LRR-RLKs: R.E.D.; Visualization: P.P-H., R.E.D.; Writing - updated manuscript: P.P-H; Review and editing: J.M.V.N., P.P-H., R.E.D., C.R-F., and J.N.T.; Funding Acquisition: J.M.V.N.

ACKNOWLEDGMENTS

We thank Roya Campos, Jason Goff, Carolyn Rasmussen and Patricia Springer (UCR) for helpful discussions during the course of this work and Siobhan Braybook (UCLA) for helpful guidance using MorphGraphX. We are also very grateful to Michael Guzman (UCR) for agreeing to include *wfl* in one

of his ongoing hypocotyl elongation assays as one of our last-ditch efforts to identify an abnormal phenotype for this mutant. We appreciate access to and assistance at the IIGB Genomics Core and Microscopy Core (UCR). We also thank Erin Sparks (Delaware Biotechnology Institute) for providing the NorfT version of the dpGreen Gateway compatible destination vector and Sebastien Santini (CNRS/AMU IGS UMR7256) and the PACA Bioinfo platform for the availability and management of the phylogeny.fr website.

DECLARATION OF INTERESTS

The authors declare no competing interests.

Figure 1

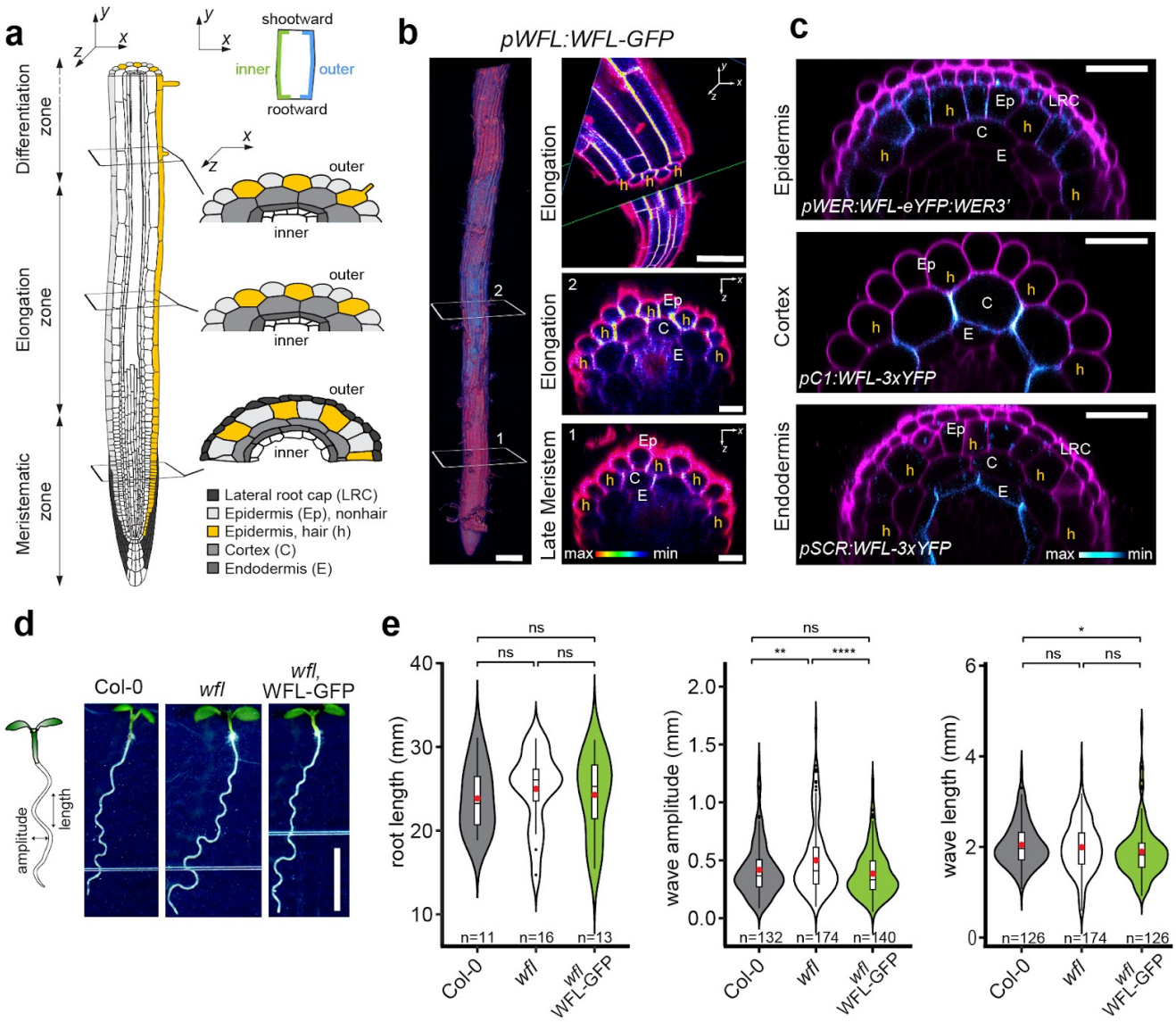

Figure 1. WFL accumulates at the inner polar domain in root cells and modulates root waving. **a,** Schematic representation of the Arabidopsis root tip with developmental zones and outermost cell types shown in (left) longitudinal and (right) transverse views. Epidermal hair (yellow) and non-hair (light gray) cells are indicated along with inner and outer polar domains. (Upper schematic) Four polarity domains represented in a single cell with lateral domains highlighted. **b**, Confocal images of a root expressing *pWFL::WFL-GFP* stained with propidium iodide (PI, magenta, GFP shown with intensity scale). *Left*, 3D projection shows higher accumulation of WLF-GFP in the elongation zone and numbered white boxes mark positions for *xz* images at right. Scale bar = 100 µm. *Right*, (top panel) intersecting *xz-xy* planes and (center and lower panels) *xz* planes show WFL-GFP in all epidermal cells in the elongation zone and primarily in hair cells in the meristematic zone. Scale bars = 100 (top) and 10 µm (center and lower) images. **c**, Confocal images of roots in *xz* planes stained with PI (magenta) and misexpressing WFL-GFP (intensity scale) under cell layer-specific promoters: *pWEREWOLF* (*pWER*) in the LRC and epidermis, *pSCARECROW* (*pSCR*) in the endodermis), *pCORTEX1* (*pC1*) in maturing cortex. Scale bars = 20 µm. **d**, *Left*, Schematic of root waving with wave amplitude and length

indicated. *Right,* Representative images of 5 day-post-stratification (dps) Arabidopsis seedlings grown on plates at 20˚ inclination. Scale bar = 0.5 cm. **e**, Quantification of root length and wave features for a single representative replicate (of 3) for Col-0, *wfl*, and *wfl* WFL-GFP. Violin plots show data distribution with box plots indicating the first and third quartiles and dots showing outliers. The median and average values are shown by a line and a red dot, respectively. Unpaired two-tailed *t*-test with Welch's correction with ns = no significance (p-value > 0.05), * (p-value < 0.05), ** (p-value < 0.01), and **** (p-value < 0.0001). See also Figure S1 and Table S1.

Figure 2

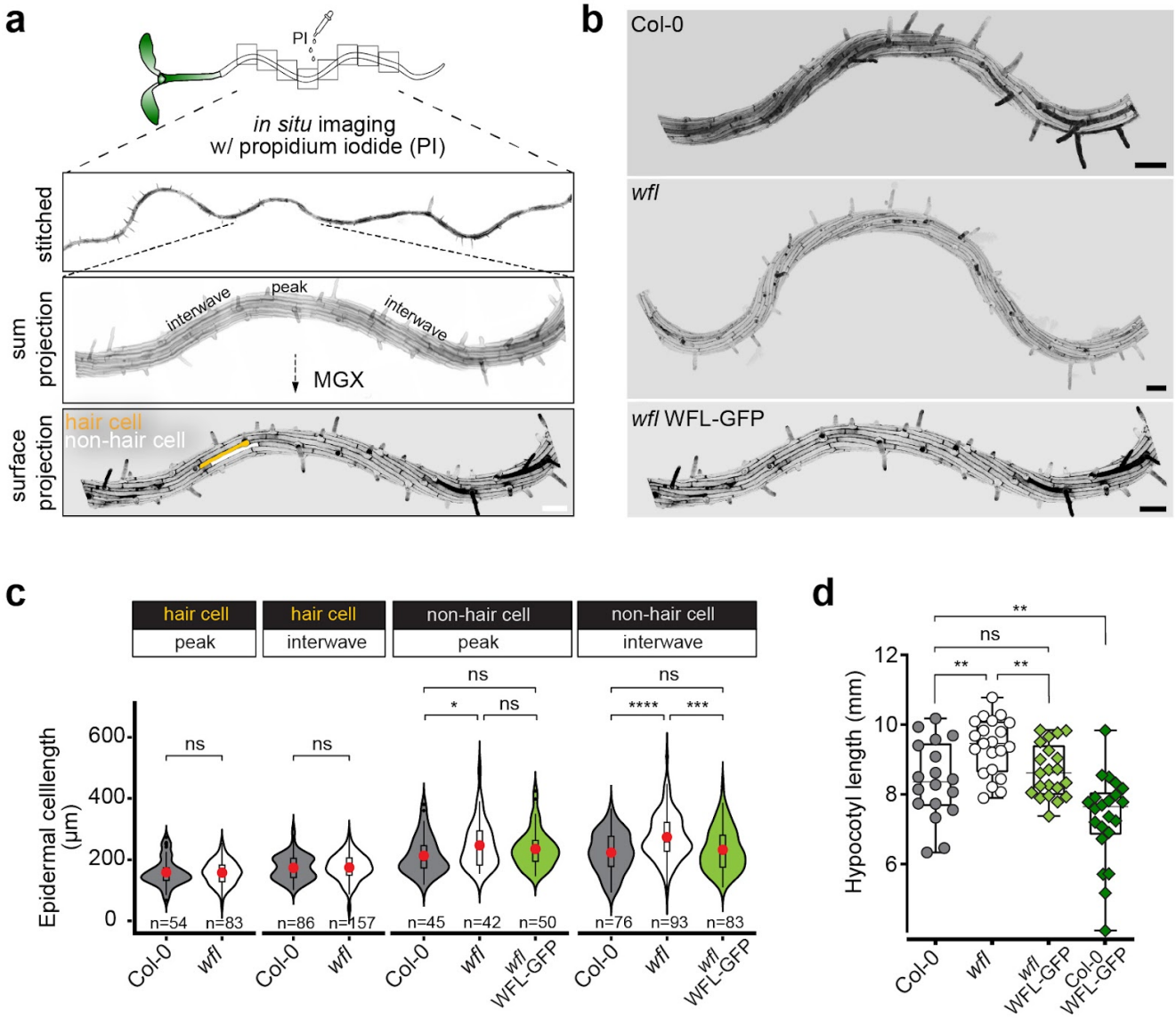

Figure 2. WFL represses elongation of root epidermal cells.

a, Schematic of *in situ* imaging approach for epidermal cell measurements within root waves. Roots were stained with propidium iodide (PI) *in situ* (without removing seedlings from the plate). Then, z-stack confocal images are obtained along the root's length in tiles (squares); then, stitched together to reconstruct a larger, continuous image area (upper root image). Root waves were divided into curved peak and straighter interwave regions. PI can be visualized by Sum (center root image) or Surface (lower root image) projections. In surface projections, obtained with MorphoGraphX (MGX), the PI fluorescence is projected onto a surface mesh, which allows clear delineation of epidermal hair (yellow) and non-hair (white) cells. Scale bar = 100 µm. **b,** Surface projections for *in situ* imaging of Col-0, *wfl*, and *wfl pWFL:WFL:GFP* roots. Scale bar = 100 µm. Seedlings were grown on tilted (20°) plates and imaged at 5 dps. **c**, Quantification of epidermal cell length in each genotype with number of cells indicated. Violin plots show data distribution with box plots indicating the first and third quartiles and median and average values indicated with a line and red dot, respectively. Unpaired two-tailed *t*-test. ns = no significance (p-value > 0.05), * (p-value < 0.05), and **** (p-value < 0.0001). **d**,

Quantification of hypocotyl length in Col-0, *wfl*, *wfl* WFL-GFP*,* and Col-0 WFL-GFP. Box plots show all data points and the box indicates the first and third quartiles, with the median value indicated as a horizontal line. Unpaired two-tailed *t*-test. ns = no significance (p-value > 0.05), ** (p-value < 0.01). See also Figure S2.

Figure 3

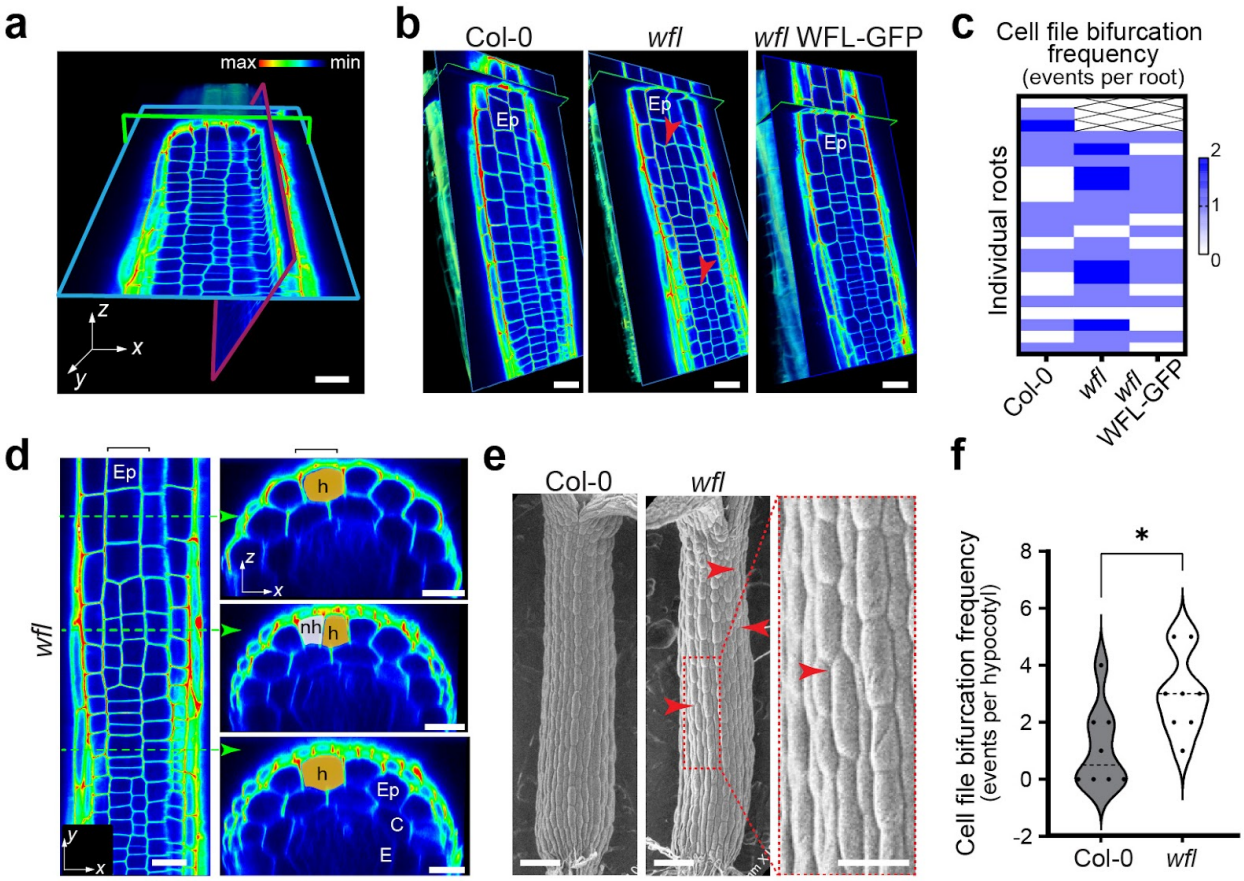

605

606 **Figure 3. *wfl* roots and hypocotyls show additional divisions in epidermal cell files.**
607 **a**, **b**, 3D confocal images of PI stained roots (intensity color scale). **a,** Image displaying the clipped
608 planes for views in *xy* (blue outline), *xz* (green outline), and *yz* (red outline). Scale bar = 20 µm. **b**,
609 Epidermal (*xy*) plane of roots with longitudinal anticlinal divisions (LADs, red arrowheads) that bifurcate
610 an epidermal cell file to produce another (partial) cell file. Scale bar = 20 µm. **c**, Heatmap showing
611 frequency of epidermal cell files bifurcation events in each genotype (n = 19-22 roots per genotype).
612 Values from aggregated data in three independent experiments. Unpaired two-tailed *t*-test shows
613 average frequency of these events in *wfl* is significantly higher (p-value < 0.01) than Col-0 or *wfl*
614 WFL-GFP. **d**, *Left*, image of *wfl* root epidermis in the longitudinal axis, with green dotted arrows
615 indicating the position of the transverse sections at right. (Lower and upper panels) A hair cell (h,
616 yellow) indicated by contact with 2 underlying cortex cells undergoes an LAD to produce a non-hair cell
617 (nh, pink, center panel) that contacts only one underlying cortex cell. Black brackets indicate the
618 epidermal cell file of interest in the *xy* (left) and *xz* (right) planes. Scale bars = 20 and 10 µm for *xy* and
619 *xz* planes, respectively. **e**, Scanning electron microscope (SEM) images of hypocotyls at 3 dps in Col-0
620 and *wfl* with bifurcation events in epidermal cell files indicated (red arrowheads). Representative
621 images (n = 8-9 hypocotyls per genotype). Scale bar = 100 µm for whole hypocotyls and 50 µm for
622 zoomed-in image. **f**, Frequency of epidermal bifurcation events in hypocotyls (events per hypocotyl, n =
623 8-9 per genotype). Violin plot shows all data points with the median indicated by dashed line. Unpaired
624 two-tailed *t*-test, * (p-value < 0.05). See also Figure S3.

625

Figure 4

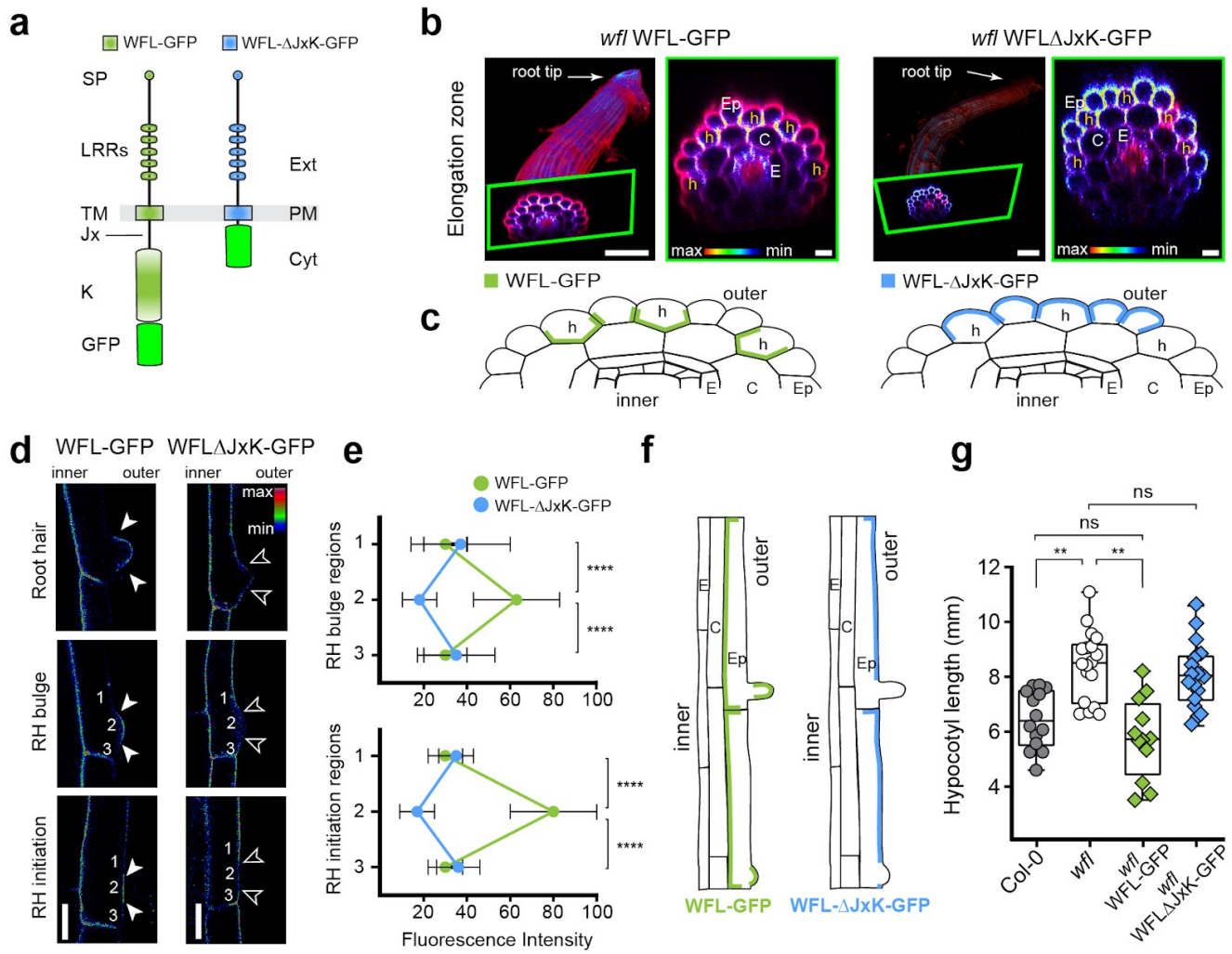

Figure 4. The WFL kinase domain is required for its localization and function.
a, Schematics of protein domains for full length WFL (green) and truncated WFLΔJxK (blue). The transmembrane (TM) domain spans the plasma membrane (PM) separating the extracellular (Ext) signal peptide (SP) and leucine-rich repeat (LRR) domains from the cytoplasmic (Cyt) juxtamembrane (Jx) and kinase (K) domains. **b**, Image of roots stained with propidium iodide (PI, magenta). (Left panels) 3D projections and (right panels) *xz* planes are shown for each genotype. Scale bars = 50 µm and 10 µm, for left and right images, respectively. **c**, Schematic representations of WFL-GFP (green) and WFLΔJxK-GFP (blue) epidermal accumulation in the transverse root axis. **d**, Confocal images during root hair (RH) formation of WFL-GFP and WFLΔJxK-GFP accumulation (in Col-0, shown with intensity color scale). Empty and filled arrowheads indicate the absence and presence of reporter accumulation, respectively. Numbers denote positions above (1), at the center (2), and below (3) RH initiation and bulge sites where fluorescence intensity was measured. Scale bar = 20 µm. **e**, Fluorescence intensity measured at the outer polar domain at positions indicated (**d**). Plots show mean values ± SD. t-test, **** $p<0.0001$. N = 15-20 roots per genotype, 2-3 cells per root. **f**, Schematic representations of WFL-GFP (green) and WFLΔJxK-GFP (blue) polar accumulation in root hair cells in the longitudinal axis. **g**, Quantification of hypocotyl elongation in various genotypes. Box plots show all the data points with the box indicating the first and third quartiles, and median value shown as a

horizontal line. Unpaired two-tailed *t*-test. ns = no significance (p-value > 0.05), ** (p-value < 0.01). See also Figure S5.

Figure 5

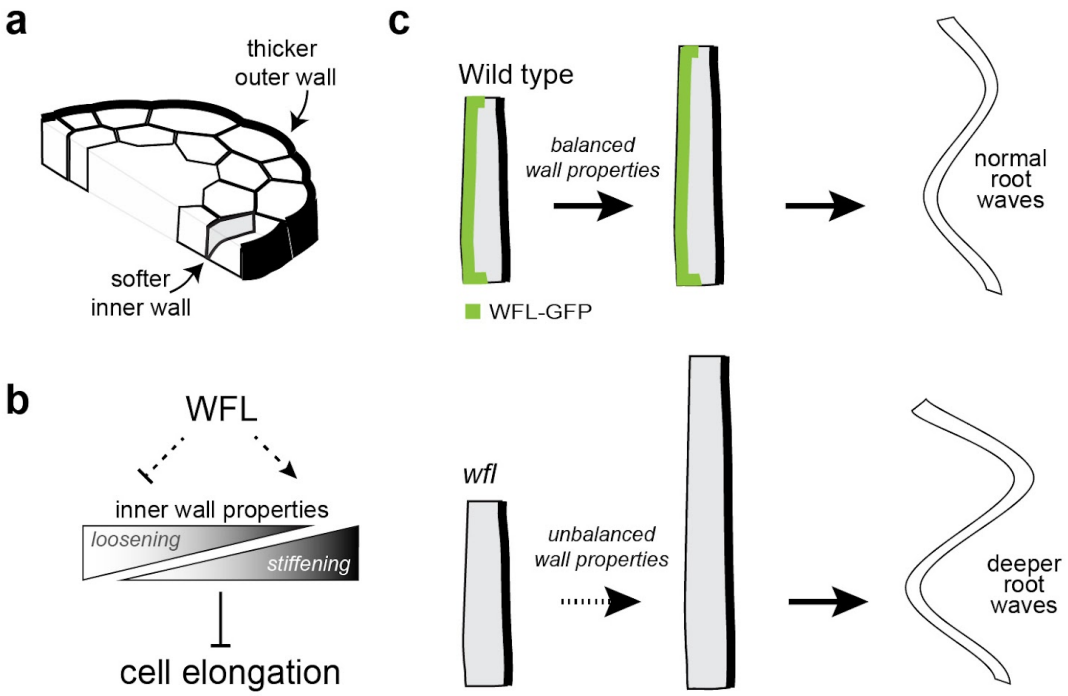

Figure 5. Model for WFL function in modulating cell elongation.
a, Schematic of transverse section of an Arabidopsis root showing differences between the inner (light gray) and outer (black) cell walls of epidermal cells (Kelly-Bellow et al., 2023). **b**, Proposed function for WFL in repression of cell elongation. Dashed lines reflect the hypothesis that WFL functions to modify inner cell wall properties to ultimately repress longitudinal cell expansion, which could occur either by directly promoting stiffness or inhibiting loosening locally at the inner wall. **c**, Schematic representation of WFL polar accumulation and impact on non-hair epidermal cell elongation and root waving. We propose WFL activity (green stripe at the inner polar domain) would balance wall properties between the inner and outer wall during cell elongation resulting in shorter cells and normal root waving. In *wfl* mutants, correct balance between inner and outer wall properties is not achieved leading to increased cell elongation and deeper root waving.

REFERENCES

Alassimone, J., Fujita, S., Doblas, V. G., Dop, M. van, Barberon, M., Kalmbach, L., Vermeer, J. E. M., Rojas-Murcia, N., Santuari, L., Hardtke, C. S., et al. (2016). Polarly localized kinase SGN1 is required for Casparian strip integrity and positioning. *Nat. Plants* **2**:16113.

Bender, K. W., and Zipfel, C. (2023). Paradigms of receptor kinase signaling in plants. *Biochem. J.* **480**:835–854.

Berger, F., Haseloff, J., Schiefelbein, J., and Dolan, L. (1998). Positional information in root epidermis is defined during embryogenesis and acts in domains with strict boundaries. *Curr. Biol.* **8**:421–430.

Bouchez, D., Uyttewaal, M., and Pastuglia, M. (2024). Spatiotemporal regulation of plant cell division. *Curr. Opin. Plant Biol.* **79**:102530.

Campos, R., and Van Norman, J. M. (2021). Confocal Analysis of Arabidopsis Root Cell Divisions in 3D: A Focus on the Endodermis. *Methods Mol. Biol.* **2382**:181–207.

Campos, R., Goff, J., Rodriguez-Furlan, C., and Norman, J. M. V. (2020). The Arabidopsis Receptor Kinase IRK Is Polarized and Represses Specific Cell Divisions in Roots. *Dev Cell* **52**:183-195.e4.

Castells, E., and Casacuberta, J. M. (2007). Signalling through kinase-defective domains: the prevalence of atypical receptor-like kinases in plants. *J. Exp. Bot.* **58**:3503–3511.

Chang, J., Li, X., Shen, J., Hu, J., Wu, L., Zhang, X., and Li, J. (2024). Defects in the cell wall and its deposition caused by loss-of-function of three RLKs alter root hydrotropism in Arabidopsis thaliana. *Nat. Commun.* **15**:2648.

Clough, S. J., and Bent, A. F. (1998). Floral dip: a simplified method forAgrobacterium-mediated transformation ofArabidopsis thaliana. *Plant J* **16**:735–743.

Czechowski, T., Stitt, M., Altmann, T., Udvardi, M. K., and Scheible, W.-R. (2005). Genome-Wide Identification and Testing of Superior Reference Genes for Transcript Normalization in Arabidopsis. *Plant Physiol.* **139**:5–17.

Daher, F. B., Chen, Y., Bozorg, B., Clough, J., Jönsson, H., and Braybrook, S. A. (2018). Anisotropic growth is achieved through the additive mechanical effect of material anisotropy and elastic asymmetry. *Elife* **7**:e38161.

Denninger, P., Reichelt, A., Schmidt, V. A. F., Mehlhorn, D. G., Asseck, L. Y., Stanley, C. E., Keinath, N. F., Evers, J.-F., Grefen, C., and Grossmann, G. (2019). Distinct RopGEFs Successively Drive Polarization and Outgrowth of Root Hairs. *Curr Biol* **29**:1854-1865.e5.

Dereeper, A., Guignon, V., Blanc, G., Audic, S., Buffet, S., Chevenet, F., Dufayard, J.-F., Guindon, S., Lefort, V., Lescot, M., et al. (2008). Phylogeny.fr: robust phylogenetic analysis for the non-specialist. *Nucleic Acids Res.* **36**:W465–W469.

Dettmer, J., and Friml, J. (2011). Cell polarity in plants: when two do the same, it is not the same.... *Curr. Opin. Cell Biol.* **23**:686–696.

Dong, J., Norman, J. V., Žárský, V., and Zhang, Y. (2023). Plant cell polarity: The many facets of sidedness. *Plant Physiol.* **193**:1–5.

Dyson, R. J., Vizcay-Barrena, G., Band, L. R., Fernandes, A. N., French, A. P., Fozard, J. A., Hodgman, T. C., Kenobi, K., Pridmore, T. P., Stout, M., et al. (2014). Mechanical modelling quantifies the functional importance of outer tissue layers during root elongation and bending. *N. Phytol.* **202**:1212–1222.

Fauser, F., Schiml, S., and Puchta, H. (2014). Both CRISPR/Cas-based nucleases and nickases can be used efficiently for genome engineering in Arabidopsis thaliana. *Plant J.* **79**:348–359.

Feng, W., Kita, D., Peaucelle, A., Cartwright, H. N., Doan, V., Duan, Q., Liu, M.-C., Maman, J., Steinhorst, L., Schmitz-Thom, I., et al. (2018). The FERONIA Receptor Kinase Maintains Cell-Wall Integrity during Salt Stress through Ca2+ Signaling. *Curr. Biol.* **28**:666-675.e5.

Gao, H., Song, W., Severing, E., Vayssières, A., Huettel, B., Franzen, R., Richter, R., Chai, J., and Coupland, G. (2022). PIF4 enhances DNA binding of CDF2 to co-regulate target gene expression and promote Arabidopsis hypocotyl cell elongation. *Nat. Plants* **8**:1082–1093.

Goff, J., Rony, R. M. I. K., Ge, Z., Hajný, J., Rodriguez-Furlan, C., Friml, J., and Norman, J. M. V. (2023). PXC2, a polarized receptor kinase, functions to repress ground tissue cell divisions and restrict stele size. *bioRxiv* Advance Access published 2023, doi:10.1101/2021.02.11.429611.

Grierson, C., Nielsen, E., Ketelaarc, T., and Schiefelbein, J. (2014). Root Hairs. *Arab. Book* **12**:e0172.

Guo, X., Park, C. H., Wang, Z.-Y., Nickels, B. E., and Dong, J. (2021). A spatiotemporal molecular switch governs plant asymmetric cell division. *Nat Plants* **7**:667–680.

Han, H., Adamowski, M., Qi, L., Alotaibi, S. S., and Friml, J. (2021). PIN-mediated polar auxin transport regulations in plant tropic responses. *N. Phytol.* **232**:510–522.

Hématy, K., Sado, P.-E., Tuinen, A. V., Rochange, S., Desnos, T., Balzergue, S., Pelletier, S., Renou, J.-P., and Höfte, H. (2007). A Receptor-like Kinase Mediates the Response of Arabidopsis Cells to the Inhibition of Cellulose Synthesis. *Curr. Biol.* **17**:922–931.

Hoermayer, L., Montesinos, J. C., Trozzi, N., Spona, L., Yoshida, S., Marhava, P., Caballero-Mancebo, S., Benková, E., Heisenberg, C.-P., Dagdas, Y., et al. (2024). Mechanical forces in plant tissue matrix orient cell divisions via microtubule stabilization. *Dev. Cell* Advance Access published 2024, doi:10.1016/j.devcel.2024.03.009.

Höfler, M., Liu, X., Greb, T., and Alim, K. (2024). Mechanical forces instruct division plane orientation of

cambium stem cells during radial growth in Arabidopsis thaliana. *Curr. Biol.* **34**:5518-5531.e4.

Jaillais, Y., Bayer, E., Bergmann, D. C., Botella, M. A., Boutté, Y., Bozkurt, T. O., Caillaud, M.-C., Germain, V., Grossmann, G., Heilmann, I., et al. (2024). Guidelines for naming and studying plasma membrane domains in plants. *Nat. Plants* **10**:1172–1183.

Janacek, D. P., Kolb, M., Schulz, L., Mergner, J., Kuster, B., Glanc, M., Friml, J., Tusscher, K. ten, Schwechheimer, C., and Hammes, U. Z. (2024). Transport properties of canonical PIN-FORMED proteins from Arabidopsis and the role of the loop domain in auxin transport. *Dev. Cell* Advance Access published 2024, doi:10.1016/j.devcel.2024.09.020.

Kelly-Bellow, R., Lee, K., Kennaway, R., Barclay, J. E., Whibley, A., Bushell, C., Spooner, J., Yu, M., Brett, P., Kular, B., et al. (2023). Brassinosteroid coordinates cell layer interactions in plants via cell wall and tissue mechanics. *Science* **380**:1275–1281.

Kleine-Vehn, J., Leitner, J., Zwiewka, M., Sauer, M., Abas, L., Luschnig, C., and Friml, J. (2008). Differential degradation of PIN2 auxin efflux carrier by retromer-dependent vacuolar targeting. *Proc National Acad Sci* **105**:17812–17817.

Koncz, C., Németh, K., Rédei, G. P., and Schell, J. (1992). T-DNA insertional mutagenesis in Arabidopsis. *Plant Mol. Biol.* **20**:963–976.

Kutschera, U., and Niklas, K. J. (2007). The epidermal-growth-control theory of stem elongation: An old and a new perspective. *J. Plant Physiol.* **164**:1395–1409.

Lee, J.-Y., Colinas, J., Wang, J. Y., Mace, D., Ohler, U., and Benfey, P. N. (2006). Transcriptional and posttranscriptional regulation of transcription factor expression in Arabidopsis roots. *Proc. Natl. Acad. Sci.* **103**:6055–6060.

Man, J., Gallagher, J. P., and Bartlett, M. (2020). Structural evolution drives diversification of the large LRR-RLK gene family. *N. Phytol.* **226**:1492–1505.

Masucci, J. D., and Schiefelbein, J. W. (1994). The rhd6 Mutation of Arabidopsis thaliana Alters Root-Hair Initiation through an Auxin- and Ethylene-Associated Process. *Plant Physiol.* **106**:1335–1346.

Muroyama, A., and Bergmann, D. (2019). Plant Cell Polarity: Creating Diversity from Inside the Box. *Annu Rev Cell Dev Bi* **35**:309–336.

Nakamura, M., and Grebe, M. (2018). Outer, inner and planar polarity in the Arabidopsis root. *Curr Opin Plant Biol* **41**:46–53.

Okada, K., and Shimura, Y. (1990). Reversible Root Tip Rotation in Arabidopsis Seedlings Induced by Obstacle-Touching Stimulus. *Science* **250**:274–276.

Oliva, M., and Dunand, C. (2007). Waving and skewing: how gravity and the surface of growth media

affect root development in Arabidopsis. *New Phytol* **176**:37–43.

Pan, X., Pérez-Henríquez, P., Norman, J. M. V., and Yang, Z. (2023). Membrane nanodomains: Dynamic nanobuilding blocks of polarized cell growth. *Plant Physiol.* **193**:83–97.

Pérez-Henríquez, P., Nagawa, S., Liu, Z., Pan, X., Michniewicz, M., Tang, W., Rasmussen, C., Cui, X., Norman, J. V., Strader, L., et al. (2025). PIN2-mediated self-organizing transient auxin flow contributes to auxin maxima at the tip of Arabidopsis cotyledons. *Nat. Commun.* **16**:1380.

Pfister, A., Barberon, M., Alassimone, J., Kalmbach, L., Lee, Y., Vermeer, J. E., Yamazaki, M., Li, G., Maurel, C., Takano, J., et al. (2014). A receptor-like kinase mutant with absent endodermal diffusion barrier displays selective nutrient homeostasis defects. *Elife* **3**:e03115.

Porat, A., Tekinalp, A., Bhosale, Y., Gazzola, M., and Meroz, Y. (2024). On the mechanical origins of waving, coiling and skewing in Arabidopsis thaliana roots. *Proc. Natl. Acad. Sci.* **121**:e2312761121.

Raggi, S., Demes, E., Liu, S., Verger, S., and Robert, S. (2020). Polar expedition: mechanisms for protein polar localization. *Curr. Opin. Plant Biol.* **53**:134–140.

Ramalho, J. J., Jones, V. A. S., Mutte, S., and Weijers, D. (2021). Pole position: How plant cells polarize along the axes. *Plant Cell* **34**:174–192.

Robbins, N. E., and Dinneny, J. R. (2018). Growth is required for perception of water availability to pattern root branches in plants. *Proc. Natl. Acad. Sci.* **115**:E822–E831.

Rodriguez-Furlan, C., Minina, E. A., and Hicks, G. R. (2019). Remove, Recycle, Degrade: Regulating Plasma Membrane Protein Accumulation. *Plant Cell* **31**:2833–2854.

Rodriguez-Furlan, C., Campos, R., Toth, J. N., and Norman, J. M. V. (2022). Distinct mechanisms orchestrate the contra-polarity of IRK and KOIN, two LRR-receptor-kinases controlling root cell division. *Nat. Commun.* **13**:235.

Rony, R. M. I. K., Campos, R., Pérez-Henríquez, P., and Norman, J. M. V. (2024). Outward askew endodermal cell divisions reveal INFLORESCENCE AND ROOT APICES RECEPTOR KINASE functions in division orientation. *Plant Physiol.* Advance Access published 2024, doi:10.1093/plphys/kiae419.

Sedbrook, J. C., and Kaloriti, D. (2008). Microtubules, MAPs and plant directional cell expansion. *Trends Plant Sci.* **13**:303–310.

Shahan, R., Hsu, C.-W., Nolan, T. M., Cole, B. J., Taylor, I. W., Greenstreet, L., Zhang, S., Afanassiev, A., Vlot, A. H. C., Schiebinger, G., et al. (2022). A single-cell Arabidopsis root atlas reveals developmental trajectories in wild-type and cell identity mutants. *Dev. Cell* **57**:543-560.e9.

Tan, T. H., Silverberg, J. L., Floss, D. S., Harrison, M. J., Henley, C. L., and Cohen, I. (2015). How

grow-and-switch gravitropism generates root coiling and root waving growth responses in Medicago truncatula. *Proc National Acad Sci* **112**:12938–12943.

Thompson, M. V., and Holbrook, N. M. (2004). Root-Gel Interactions and the Root Waving Behavior of Arabidopsis . *Plant Physiol* **135**:1822–1837.

Van Norman, J. M. (2016). Asymmetry and cell polarity in root development. *Dev. Biol.* **419**:165–174.

Van Norman, J. M., Zhang, J., Cazzonelli, C. I., Pogson, B. J., Harrison, P. J., Bugg, T. D. H., Chan, K. X., Thompson, A. J., and Benfey, P. N. (2014). Periodic root branching in Arabidopsis requires synthesis of an uncharacterized carotenoid derivative. *Proc National Acad Sci* **111**:E1300-9.

Vissenberg, K., Fry, S. C., and Verbelen, J.-P. (2001). Root Hair Initiation Is Coupled to a Highly Localized Increase of Xyloglucan Endotransglycosylase Action in Arabidopsis Roots. *Plant Physiol.* **127**:1125–1135.

Wheeldon, C. D., Hamon-Josse, M., Lund, H., Yoneyama, K., and Bennett, T. (2022). Environmental strigolactone drives early growth responses to neighboring plants and soil volume in pea. *Curr Biol* Advance Access published 2022, doi:10.1016/j.cub.2022.06.063.

Yi, P., Ou, G., and Li, W. (2025). Multifaceted regulation of asymmetric cell division by the actin cytoskeleton. *Curr. Opin. Cell Biol.* **94**:102491.

Yoshida, S., Schuren, A. van der, Dop, M. van, Galen, L. van, Saiga, S., Adibi, M., Möller, B., Hove, C. A. ten, Marhavy, P., Smith, R., et al. (2019). A SOSEKI-based coordinate system interprets global polarity cues in Arabidopsis. *Nat Plants* **5**:160–166.

Zhang, Z., Ophem, D. van, Chelakkot, R., Lazarovitch, N., and Regev, I. (2022). A mechano-sensing mechanism for waving in plant roots. *Sci. Rep.* **12**:9635.

FIGURE LEGENDS

Figure 1. WFL accumulates at the inner polar domain in root cells and modulates root waving.

a, Schematic representation of the Arabidopsis root tip with developmental zones and outermost cell types shown in (left) longitudinal and (right) transverse views. Epidermal hair (yellow) and non-hair (light gray) cells are indicated along with inner and outer polar domains. (Upper schematic) Four polarity domains represented in a single cell with lateral domains highlighted. **b**, Confocal images of a root expressing *pWFL::WFL-GFP* stained with propidium iodide (PI, magenta, GFP shown with intensity scale). *Left*, 3D projection shows higher accumulation of WLF-GFP in the elongation zone and numbered white boxes mark positions for *xz* images at right. Scale bar = 100 µm. *Right*, (top panel) intersecting *xz-xy* planes and (center and lower panels) *xz* planes show WFL-GFP in all epidermal cells in the elongation zone and primarily in hair cells in the meristematic zone. Scale bars = 100 (top) and 10 µm (center and lower) images. **c**, Confocal images of roots in *xz* planes stained with PI (magenta) and misexpressing WFL-GFP (intensity scale) under cell layer-specific promoters: *pWEREWOLF* (*pWER*) in the LRC and epidermis, *pSCARECROW* (*pSCR*) in the endodermis), *pCORTEX1* (*pC1*) in maturing cortex. Scale bars = 20 µm. **d**, *Left*, Schematic of root waving with wave amplitude and length indicated. *Right,* Representative images of 5 day-post-stratification (dps) Arabidopsis seedlings grown on plates at 20˚ inclination. Scale bar = 0.5 cm. **e**, Quantification of root length and wave features for a single representative replicate (of 3) for Col-0, *wfl*, and *wfl* WFL-GFP. Violin plots show data distribution with box plots indicating the first and third quartiles and dots showing outliers. The median and average values are shown by a line and a red dot, respectively. Unpaired two-tailed *t*-test with Welch's correction with ns = no significance (p-value > 0.05), * (p-value < 0.05), ** (p-value < 0.01), and **** (p-value < 0.0001). See also Figure S1 and Table S1.

Figure 2. WFL represses elongation of root epidermal cells.

a, Schematic of *in situ* imaging approach for epidermal cell measurements within root waves. Roots were stained with propidium iodide (PI) *in situ* (without removing seedlings from the plate). Then, z-stack confocal images are obtained along the root's length in tiles (squares); then, stitched together to reconstruct a larger, continuous image area (upper root image). Root waves were divided into curved peak and straighter interwave regions. PI can be visualized by Sum (center root image) or Surface (lower root image) projections. In surface projections, obtained with MorphoGraphX (MGX), the PI fluorescence is projected onto a surface mesh, which allows clear delineation of epidermal hair (yellow) and non-hair (white) cells. Scale bar = 100 µm. **b,** Surface projections for *in situ* imaging of Col-0, *wfl*, and *wfl pWFL:WFL:GFP* roots. Scale bar = 100 µm. Seedlings were grown on tilted (20°) plates and imaged at 5 dps. **c**, Quantification of epidermal cell length in each genotype with number of cells indicated. Violin plots show data distribution with box plots indicating the first and third quartiles and median and average values indicated with a line and red dot, respectively. Unpaired two-tailed *t*-test. ns = no significance (p-value > 0.05), * (p-value < 0.05), and **** (p-value < 0.0001). **d**, Quantification of hypocotyl length in Col-0, *wfl*, *wfl* WFL-GFP*,* and Col-0 WFL-GFP. Box plots show all data points and the box indicates the first and third quartiles, with the median value indicated as a horizontal line. Unpaired two-tailed *t*-test. ns = no significance (p-value > 0.05), ** (p-value < 0.01). See also Figure S2.

Figure 3. *wfl* roots and hypocotyls show additional divisions in epidermal cell files.

a, **b**, 3D confocal images of PI stained roots (intensity color scale). **a,** Image displaying the clipped planes for views in *xy* (blue outline), *xz* (green outline), and *yz* (red outline). Scale bar = 20 µm. **b**,

Epidermal (*xy*) plane of roots with longitudinal anticlinal divisions (LADs, red arrowheads) that bifurcate an epidermal cell file to produce another (partial) cell file. Scale bar = 20 µm. **c**, Heatmap showing frequency of epidermal cell files bifurcation events in each genotype (n = 19-22 roots per genotype). Values from aggregated data in three independent experiments. Unpaired two-tailed *t*-test shows average frequency of these events in *wfl* is significantly higher (p-value < 0.01) than Col-0 or *wfl* WFL-GFP. **d**, *Left*, image of *wfl* root epidermis in the longitudinal axis, with green dotted arrows indicating the position of the transverse sections at right. (Lower and upper panels) A hair cell (h, yellow) indicated by contact with 2 underlying cortex cells undergoes an LAD to produce a non-hair cell (nh, pink, center panel) that contacts only one underlying cortex cell. Black brackets indicate the epidermal cell file of interest in the *xy* (left) and *xz* (right) planes. Scale bars = 20 and 10 µm for *xy* and *xz* planes, respectively. **e**, Scanning electron microscope (SEM) images of hypocotyls at 3 dps in Col-0 and *wfl* with bifurcation events in epidermal cell files indicated (red arrowheads). Representative images (n = 8-9 hypocotyls per genotype). Scale bar = 100 µm for whole hypocotyls and 50 µm for zoomed-in image. **f**, Frequency of epidermal bifurcation events in hypocotyls (events per hypocotyl, n = 8-9 per genotype). Violin plot shows all data points with the median indicated by dashed line. Unpaired two-tailed *t*-test, * (p-value < 0.05). See also Figure S3.

Figure 4. The WFL kinase domain is required for its localization and function.

a, Schematics of protein domains for full length WFL (green) and truncated WFLΔJxK (blue). The transmembrane (TM) domain spans the plasma membrane (PM) separating the extracellular (Ext) signal peptide (SP) and leucine-rich repeat (LRR) domains from the cytoplasmic (Cyt) juxtamembrane (Jx) and kinase (K) domains. **b**, Image of roots stained with propidium iodide (PI, magenta). (Left panels) 3D projections and (right panels) *xz* planes are shown for each genotype. Scale bars = 50 µm and 10 µm, for left and right images, respectively. **c**, Schematic representations of WFL-GFP (green) and WFLΔJxK-GFP (blue) epidermal accumulation in the transverse root axis. **d**, Confocal images during root hair (RH) formation of WFL-GFP and WFLΔJxK-GFP accumulation (in Col-0, shown with intensity color scale). Empty and filled arrowheads indicate the absence and presence of reporter accumulation, respectively. Numbers denote positions above (1), at the center (2), and below (3) RH initiation and bulge sites where fluorescence intensity was measured. Scale bar = 20 µm. **e**, Fluorescence intensity measured at the outer polar domain at positions indicated (**d**). Plots show mean values ± SD. t-test, **** p<0.0001. N = 15-20 roots per genotype, 2-3 cells per root. **f**, Schematic representations of WFL-GFP (green) and WFLΔJxK-GFP (blue) polar accumulation in root hair cells in the longitudinal axis. **g**, Quantification of hypocotyl elongation in various genotypes. Box plots show all the data points with the box indicating the first and third quartiles, and median value shown as a horizontal line. Unpaired two-tailed *t*-test. ns = no significance (p-value > 0.05), ** (p-value < 0.01). See also Figure S5.

Figure 5. Model for WFL function in modulating cell elongation.

a, Schematic of transverse section of an Arabidopsis root showing differences between the inner (light gray) and outer (black) cell walls of epidermal cells (Kelly-Bellow et al., 2023). **b**, Proposed function for WFL in repression of cell elongation. Dashed lines reflect the hypothesis that WFL functions to modify inner cell wall properties to ultimately repress longitudinal cell expansion, which could occur either by directly promoting stiffness or inhibiting loosening locally at the inner wall. **c**, Schematic representation of WFL polar accumulation and impact on non-hair epidermal cell elongation and root waving. We

propose WFL activity (green stripe at the inner polar domain) would balance wall properties between the inner and outer wall during cell elongation resulting in shorter cells and normal root waving. In *wfl* mutants, correct balance between inner and outer wall properties is not achieved leading to increased cell elongation and deeper root waving.

963 **SUPPLEMENTAL INFORMATION**

Figure S1

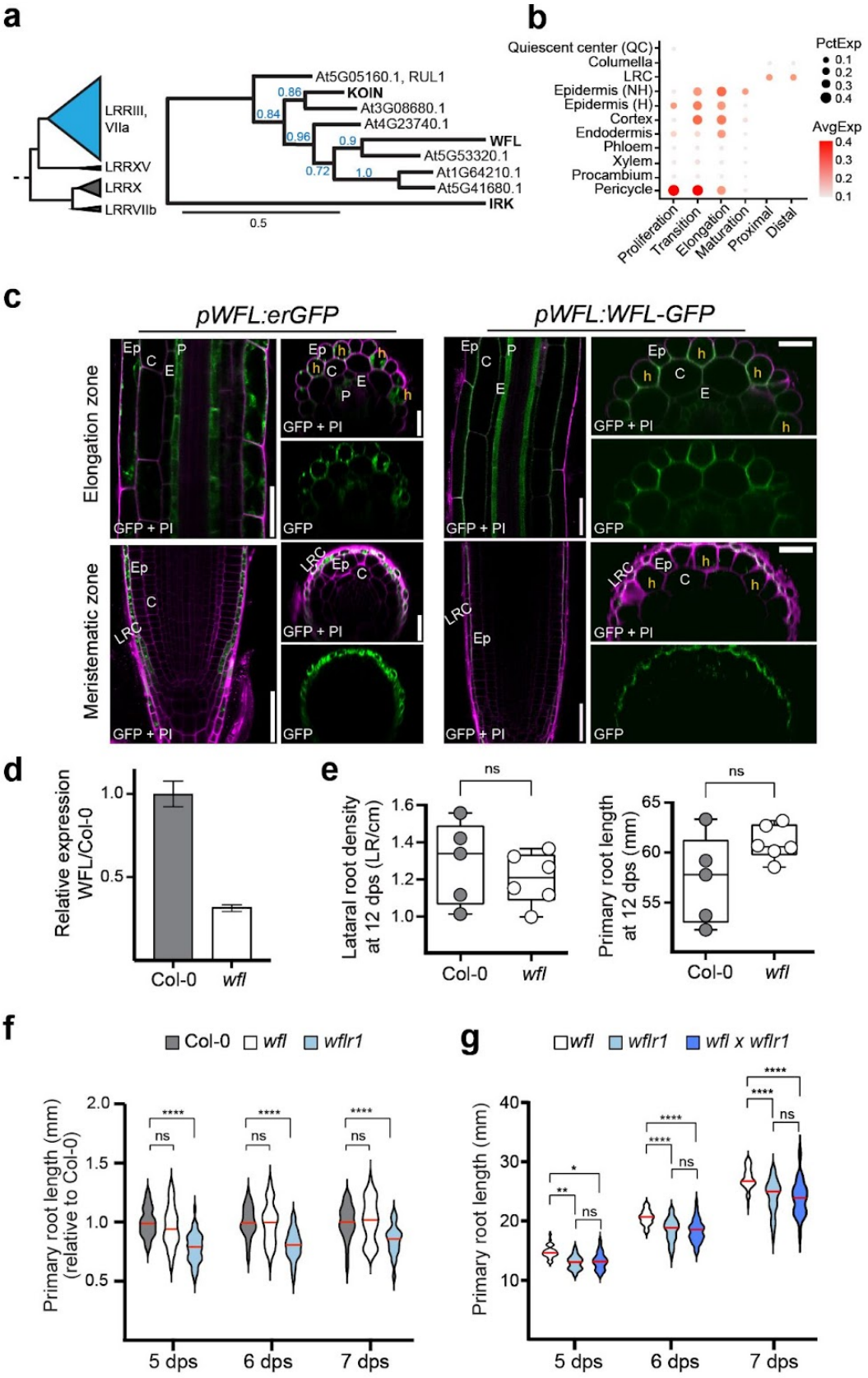

964

Figure S1. *WFL* promoter activity and protein accumulation and various phenotypic assays.
a, *Left*, Partial phylogenetic tree adapted from (Man et al., 2020) with only Arabidopsis proteins included. Triangles drawn to scale to represent the number of proteins included: LRRIII, VIIa - 54; LRRXV - 2, LRRX - 11, and LRRVIIb - 3. Subgroup LRRIII, VIIa (blue) contains WFL and several other Arabidopsis LRR-RLKs with polar accumulation in root cell types, including KOIN (At5g53800 Rodriguez-Furlan et al., 2022) and IRK (Campos et al., 2020). *Right*, Unrooted phylogram with bootstrap support values in blue. Members of the LRRIII/VIIa subgroup, including KOIN (At5G53800) and WFL (At5G24100) from LRRIII, with IRK (At3G56370) included as a more distantly related subfamily member (representing VIIa members). Legend shows branch length 0.5. Phylogram built at https://www.phylogeny.fr/alacarte.cgi using "a la carte mode" (Dereeper et al., 2008). **b**, *WFL* mRNA expression data from atlas ARVEX - https://shiny.mdc-berlin.de/ARVEX (Shahan et al., 2022). Color intensity represents *WFL* expression level (AvgExp), and dot size depicts the percentage of cells with that expression (PctExp). **c**, Roots stained with propidium iodide (PI, magenta) expressing (*Left panels*) *pWFL:erGFP* and (*Right panels*) *pWFL:WFL-GFP*. Adjacent panels show GFP alone (Green) or GFP + PI signal in the meristematic and elongation zones. **d,** RT-qPCR shows reduced *WFL* transcript levels with 3 technical replicates conducted per biological replicate (of 3) with similar results obtained in all. Plot shows mean ± SEM. **e**, Emerged lateral root density (LR number / primary root length) and corresponding primary root length measured in Col-0 and *wfl* seedlings at 12 dps. **f**, Primary root length of *wfl* and *wfl-r1* (At5G53320) roots relative to Col-0 at 5, 6, and 7 days post-stratification (dps). Violin plot shows the data and distribution of all data points relative to the average of Col-0 at each day. Median is a red horizontal line. One-way ANOVA with Dunn's multiple comparisons test. Col-0: 5dps n=81, 6dps n=66, 7dps n=51; *wfl*: 5dps n=70, 6dps n=58, 7dps n=44; *wflr1*: 5-7dps n=34. **** (p-value < 0.0001). **g**, Primary root length *wfl*, *wflr1,* and *wfl wflr1* double mutants at 5, 6, 7 dps. Violin plot shows data distribution and the median value as a red horizontal line. One-way ANOVA with Dunn's multiple comparisons test. *wfl*: 5dps n=68, 6dps n=54, 7dps n=44; *wflr1*: 5dps n=59, 6dps n=53, 7dps n=43; *wfl wflr1*: 5dps n=64, 6dps n=53, 7dps n=41. ns = no significance (p-value > 0.05), * (p-value = 0.0335), ** (p-value = 0.0033), **** (p-value < 0.0001).

Figure S2

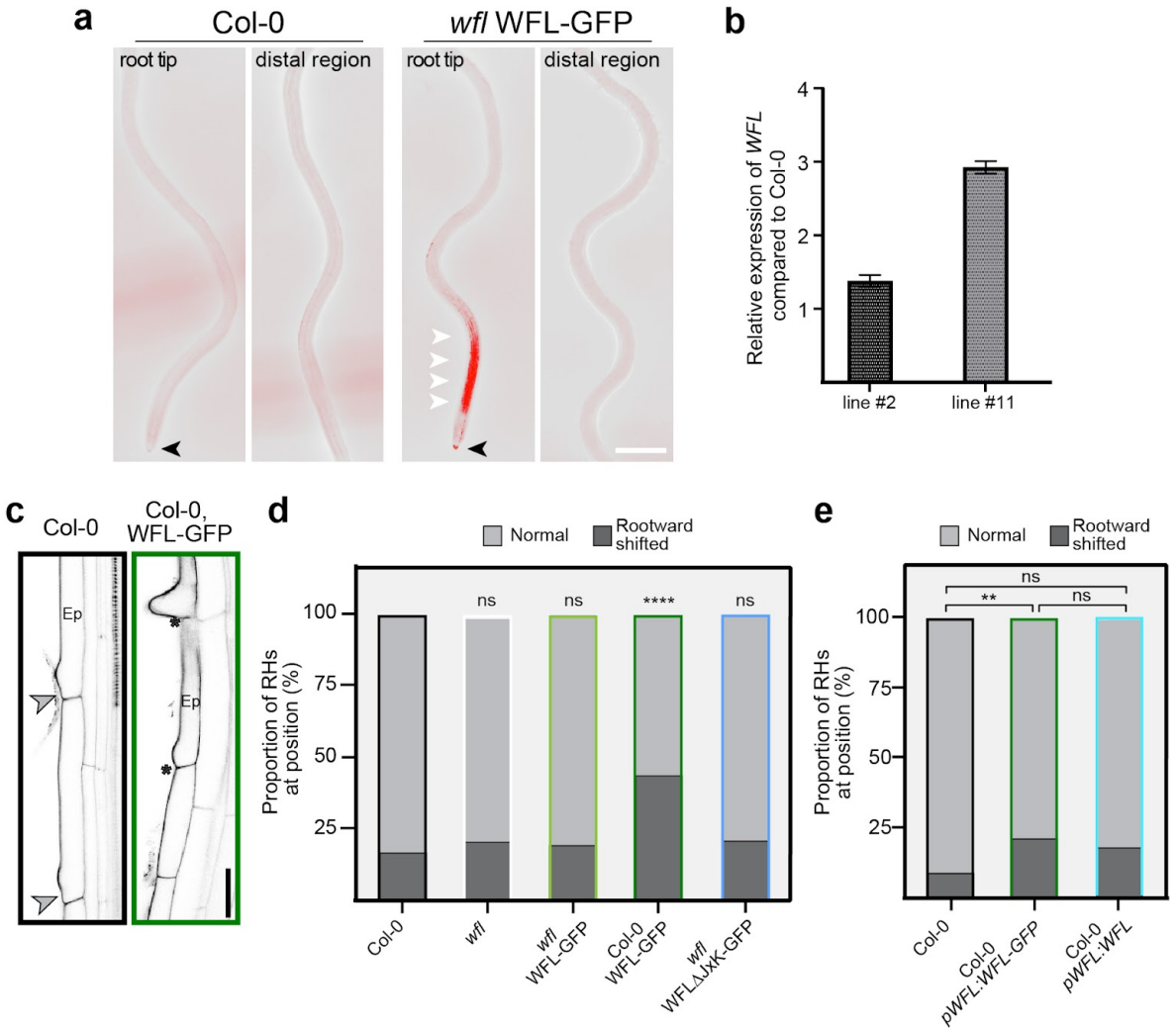

Figure S2. WFL-GFP accumulates strongly in the elongation zone and root hair positioning is impacted by *WFL* overexpression.

a, Wild type (Col-0) and *wfl pWFL::WFL-GFP* seedlings at 5 dps grown on tilted (20˚) plates and imaged with fluorescence microscopy (GFP displayed in red). White arrowheads indicate strong WFL-GFP signal at the root elongation zone. Black arrowheads indicate root apices. Scale bar = 0.5 mm.

b, *WFL* transcript levels in two independent overexpression lines (Col-0, *pWFL::WFL-GFP*). *WFL* relative expression was measured by RT-qPCR relative to the expression in Col-0. Plot shows mean ± SEM. **c,** Confocal images of root hair cells in Col-0 and Col-0 *pWFL:WFL:GFP*. Gray arrowhead indicates normal gap between the root hair and the rootward end of the cell. Asterisk indicates absence of a gap. **d**, Proportion of root hairs classified as normally positioned (light grey) or shifted downwards (dark grey) in different genetic backgrounds. *t*-test, ns= not significant (p>0.05), ** p<0.01, and **** p<0.0001. (n= 15 roots). **e,** Proportion of root hairs classified as normally positioned (light grey) or shifted downwards (dark grey) in Col-0 and Col-0 expressing WFL with and without GFP.

Figure S3

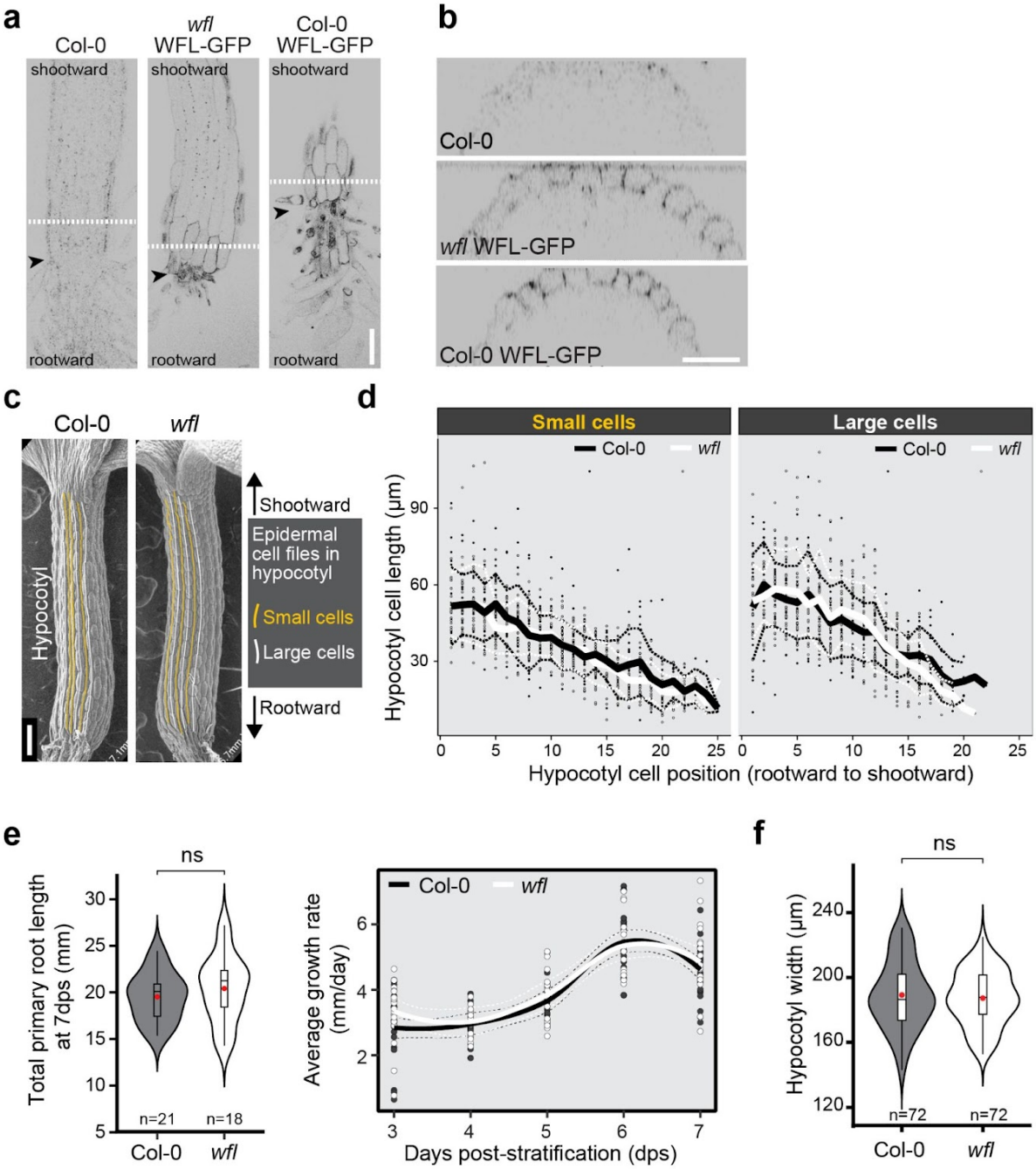

Figure S3. Loss of *WFL* does not affect hypocotyl width or epidermal cell length in normal light conditions.

a-b, Confocal images of WFL-GFP in Col-0 and *wfl* seedlings at 2.5 dps. **a**, Longitudinal optical sections (*xy* planes) at the surface of hypocotyls. Black arrowhead indicates root-hypocotyl junction and white dashed line indicates position of transverse optical sections in **b**. Scale bar = 60 µm. **b**, Transverse optical sections (*xz* planes) at positions in **a**. Scale bar = 60 µm. **c**, Scanning electron microscopy (SEM) images from Col-0 and *wfl* hypocotyls at 3 dps allows for discrimination between small (yellow vertical lines) and large cells (white vertical lines) and measurement of their lengths. Scale bar = 100 µm. **d**, Scatter plot of hypocotyl epidermal cell length arranged by their position (rootward to shootward). Graph

shows individual data points with mean value (thick line) and standard deviation (dashed lines). n= 886 and 922 cells for Col-0 and *wfl*, respectively. **e**, Total root length and root growth rate from seedlings grown on media without sucrose (same growth conditions for hypocotyl assays). *Left panel*, Total primary root length at 7 dps. Violin plot shows data distribution with the box plots indicating the first and third quartiles and median and average values shown with a line and red dot, respectively. Unpaired two-tailed *t*-test. No statistically significant difference (ns, p-value > 0.05). *Right panel*, Corresponding root growth rates. Graph shows individual data points with mean value (thick line) and standard deviation (dashed lines). **f**, Hypocotyl width of *Col-0* and *wfl* seedlings at 3 dps. The violin plot shows data distribution with the box plot indicating the first and third quartiles, the median value shown by a line, and the average by a red dot. Unpaired two-tailed *t*-test with Welch's correction. No statistically significant difference (ns, p-value > 0.05).

Figure S4

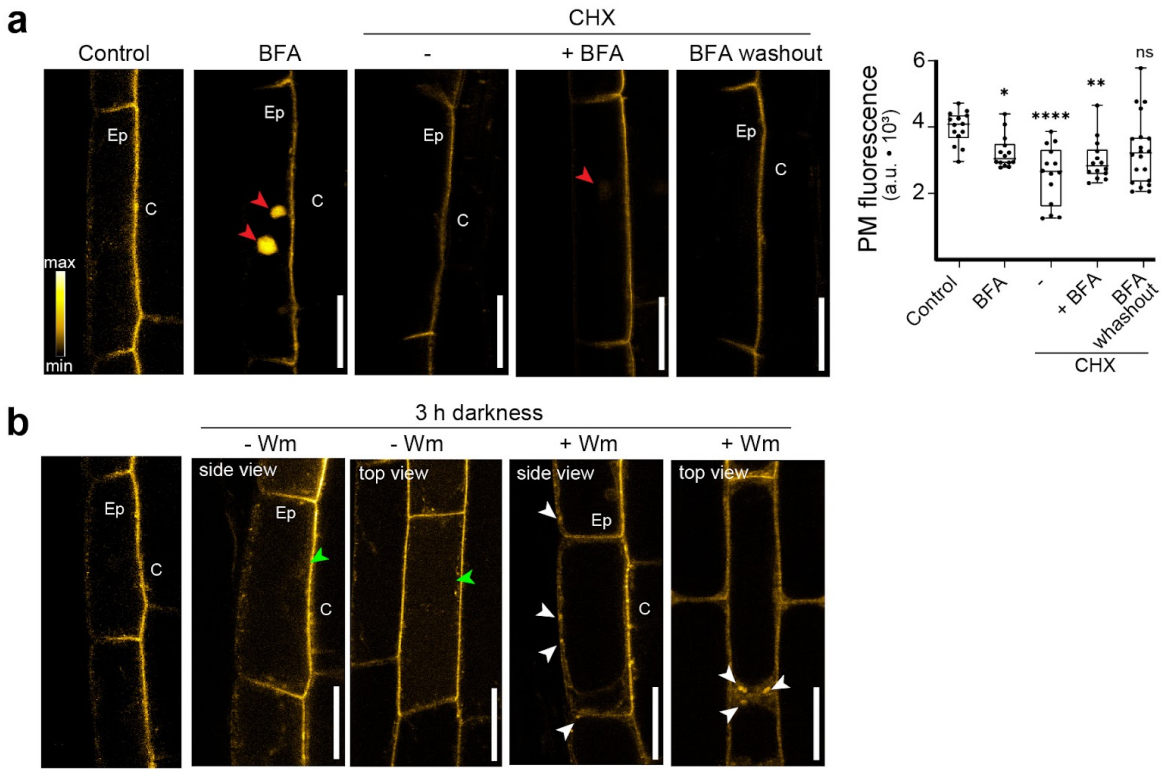

Figure S4. WFL is rapidly trafficked to and from the plasma membrane (PM).
a, **b**, Confocal images of root epidermal cells expressing WFL-GFP. **a**, *Left-to-right,* Solvent control. Upon treatment with BrefeldinA (BFA, 1h), intracellular aggregates are detectable (red arrows). Treatment with protein synthesis inhibitor cycloheximide (CHX, 2h) reduces PM fluorescence and co-treatment (+ BFA) inhibits WFL-GFP accumulation in BFA-bodies. Removal of BFA in the presence of CHX (BFA washout) restored protein levels at the PM. *Right*, Quantification of GFP intensity at the PM after each treatment. Representative data shown from one of three independent replicates. The box plot shows all the data points with the box indicating the first and third quartiles and the horizontal line denotes the median. One-way ANOVA with Dunn's multiple comparison test. ns= not significant ($p>0.05$), * $p<0.05$, ** $p<0.01$, and **** $p<0.0001$ **b**, *Left-to-right,* Solvent control (side view only). WFL-GFP trafficks to the vacuole after 3h dark treatment (green arrowheads), and this trafficking is inhibited by Wortmanin (Wm), resulting in aggregated WFL-GFP in the prevacuolar compartment (white arrowheads).

Figure S5

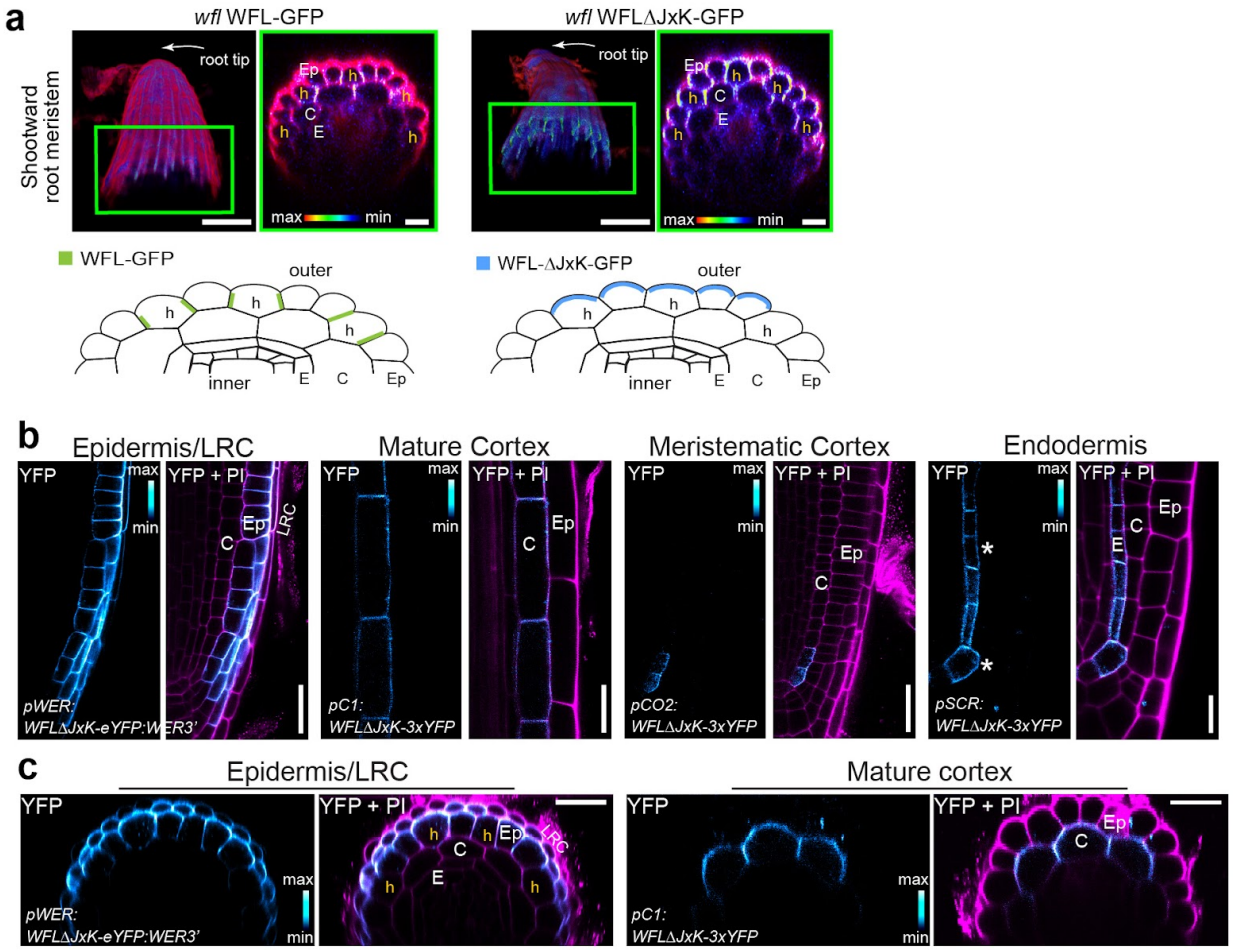

Figure S5. WFLΔJxK-GFP predominantly localizes to the outer polar domain of root cell types. **a**, *Upper panels*, Confocal images of the shootward portion of root meristems stained with propidium iodide (PI, magenta). *Left*, 3D projections and (right) *xz* planes for each genotype. WFL-GFP accumulates at the circumferential polar domain of hair cells (as seen in Figure 1b), whereas WFLΔJxK-GFP accumulates at the circumferential and outer polar domains of all epidermal cells. *Lower panels*, Schematic representations of WFL-GFP (green) and WFLΔJxK-GFP (blue) accumulation in the root epidermal cells in the shootward portion of the meristematic zone. Scale bar = 50 μm and 10 μm, for left and right images, respectively. **b**-**c**, Roots expressing WFLΔJxK-eYFP/3xYFP driven by cell layer-specific promoters and stained with propidium iodide (PI, magenta). Adjacent panels show YFP alone (shown with signal intensity color scale) and YFP + PI merged in (**b**) median longitudinal planes and (**c**) transverse planes. In the ground tissue initials and endodermis of lateral roots (far right panels (**b**)), WFLΔJxK-eYFP displays nonpolar accumulation (white asterisks). Scale bars: 25 μm.

1058 **Table S1. List of primers used in this study**

Purpose	Primer Name	Sequence (5'->3')
Genotyping	WFLcod_seqF3*	GGTACTATCAGCCGTCTATCG
	WFLcod_seqR2*	ATTTCGCTCTTATCCTCCATGTC
	*Amplification followed by digestion with SacII for genotyping *wfl-1*	
	Salk_128780_LP	ATGCATCAGTGTAGCCATTCC
	Salk_128780_RP	CTCGACTTCAACGAGTTTTCG
	LBb1.3	ATTTTGCCGATTTCGGAAC
Cloning	WFLcod_F	caccATGAGTAGAGGAAGATCTTTCATCTTC
	WFLcod_R	GTCTCTCTCAATCTCTTCCAAAGTC
	WFLpro_F	CGAAGAGTCATGTTGGTCATGTT
	WFLpro_R	CTTCTTACTAATTGTTATGTGATGGA
	WFLcod_truncR	TGTCTCTGACTTCCTCTGCCT
	WFLcod_trunc-K_R	TGCAGAAGCTATCAACAAGTCTTC
qRT-PCR	WFL_ex1/2_qF	CGCATTTGAACTATATAAAAGTC
	WFL_ex2_qR2	ACAGAGCCGATGATCCAAAGA
	WFL_ex2_qF3	GCTTACGTGTGTTCCAAGGA
	WFL_ex2/3_qR1	GTCTGCGTTCTTGCCATGAA
	PP2A_qF	TAACGTGGCCAAAATGATGC
	PP2A_qR	GTTCTCCACAACCGCTTGGT

1059